Tectonophysics 817 (2021) 229042

Contents lists available at ScienceDirect

Tectonophysics

journal homepage: www.elsevier.com/locate/tecto

Passive margin inversion controlled by stability of the mantle lithosphere

A. Auzemery [a,*], E. Willingshofer [a], D. Sokoutis [a,b], J.P. Brun [c], S.A.P.L. Cloetingh [a]

[a] Utrecht University, Faculty of Geosciences, Department of Earth Sciences, the Netherlands
[b] University of Oslo, Department of Geosciences, Oslo, Norway
[c] Univ Rennes, CNRS, Géosciences Rennes-UMR 6118, Rennes, France

ARTICLE INFO

Keywords:
Margin inversion
Condition for subduction initiation
Analogue modelling
Lithosphere folding

ABSTRACT

Contractional deformation of passive continental margins may resemble early stages of induced subduction initiation. Mechanical instabilities are required to permit underthrusting of the oceanic plate. Therefore, the success of developing a new subduction zone will largely depend on the rheology of the mantle lithosphere. In this physical analogue modelling study, a range of mantle viscosities subject to different convergence rates serve as a proxy to simulate contraction of differently aged passive margins with the purpose of describing and quantifying passive margin deformation and mantle stability using the buoyancy number. The experiments illustrate distinct differences in geometry and length-scale of deformation as a function of lithospheric mantle strengths. The results indicate that deformation occurs at passive margins for intermediate strength lithospheric mantle and high strain rate. In contrast, low and high strength mantle lithospheres lead to dominantly intra-oceanic deformation or long wavelength buckling of the entire model, respectively. Our experiments portray an evolution in which early-stage deformation commences at the ocean-continent transition and is controlled by the ductile lower crust of the continent. In the next stage, shear localization through the formation of a decollement within the ductile passive margin crust favors underthrusting of the oceanic lithosphere, leading to a reduction of the area affected by deformation. Prior to underthrusting, the primary response of the lithosphere to compression is by folding at scaled wavelengths of 100–300 km and 500–1000 km, controlled by the strength of the mantle lithosphere.

1. Introduction

On earth the total length of passive continental margins is in the order of 105,000 km (Bradley, 2008). Within the frame of the Wilson cycle (Burke, 1976; Wilson, 1968), passive continental margins will eventually be turned into active margins where new subduction zones emerge. The processes contributing to this change in dynamic conditions and their structural and topographic expression are, however, not well understood. The lack of modern examples of subduction initiation along the passive margins of the Atlantic or Indian oceans, suggests that passive continental margins are stable features, promoting the idea that subduction zone invasion is required for the formation of subduction zones at continental margins (Crameri et al., 2020; Duarte et al., 2013; Zhou et al., 2020). Although observational evidences from modern examples constraining the subduction nucleation process are inconclusive, inferences from the geological record like the Alps (Manzotti et al., 2014), Ryukiu (Hall, 2019) and the eastern Pacific (McCarthy et al., 2018) suggest that subduction-initiation must have occurred at passive margins in the plate tectonics history. Deformation at passive continental margins is usually attributed to two contrasting driving mechanisms including (a) body forces arising from density contrasts or (b) far field forces (Stern, 2004). In context of the nucleation of subduction zones, these distinct forcing conditions are referred to as “spontaneous” or “induced” mechanisms of subduction initiation (Stern, 2004; Stern and Gerya, 2018). While spontaneous subduction initiation is predominantly associated with extension of the overriding plate, induced subduction initiation occurs within a contractional tectonic regime and will thus lead to shortening of the passive continental margin (Stern, 2004). For either of these mechanisms, driving forces need to overcome resisting forces among which the shear strength of the lithosphere being of critical importance (e.g. Cloetingh et al., 1989; Mueller and Phillips, 1991).

Previous studies have shown that although passive continental margins are sites of significant density contrasts and thus high buoyancy forces (Vlaar and Wortel, 1976), the nucleation of a new subduction zone by spontaneous collapse is unlikely because of the increasing shear

* Corresponding author.
E-mail address: antoine.auzemery@gmail.com (A. Auzemery).

https://doi.org/10.1016/j.tecto.2021.229042
Received 25 November 2020; Received in revised form 20 July 2021; Accepted 25 August 2021
Available online 28 August 2021

resistance of the lithosphere related to cooling (Cloetingh et al., 1982; Mueller and Phillips, 1991). In contrast, numerous examples of inverted passive margins (Johnson, 2008; Pedoja et al., 2011; Yamato et al., 2013; Ziegler and Cloetingh, 2004) suggest that subduction initiation at passive margins should predominantly be expressed by deformation of the load-bearing crustal and mantle layers within a contractional regime (Nikolaeva et al., 2010; Zhong and Li, 2019). At shallow levels, stress concentration leads to folding, reverse and thrust faulting and associated seismicity (Stein et al., 1989b; Yamato et al., 2013). While deformation of the crust is well documented, it is unclear how the mantle lithosphere at passive margins reacts to applied stresses during passive margin inversion. From a mechanical perspective, the strength of the mantle lithosphere often inhibits its failure, calling for the presence of weak mantle lithospheres (Göğüş and Pysklywec, 2008; Li et al., 2016b) or pre-existing weak zones (Stern and Gerya, 2018 and references therein) to localize strain in the lithospheric mantle. From the studies quoted above, it follows that deformation at passive margins, potentially leading to the development of a subduction zone, is strongly related to the strength and the gravitational stability of both the crust and the mantle lithosphere (Boonma et al., 2019; Faccenna et al., 1999). Although natural examples show that deformation localizes at passive continental margins, it is difficult to predict if an inverted passive margin will

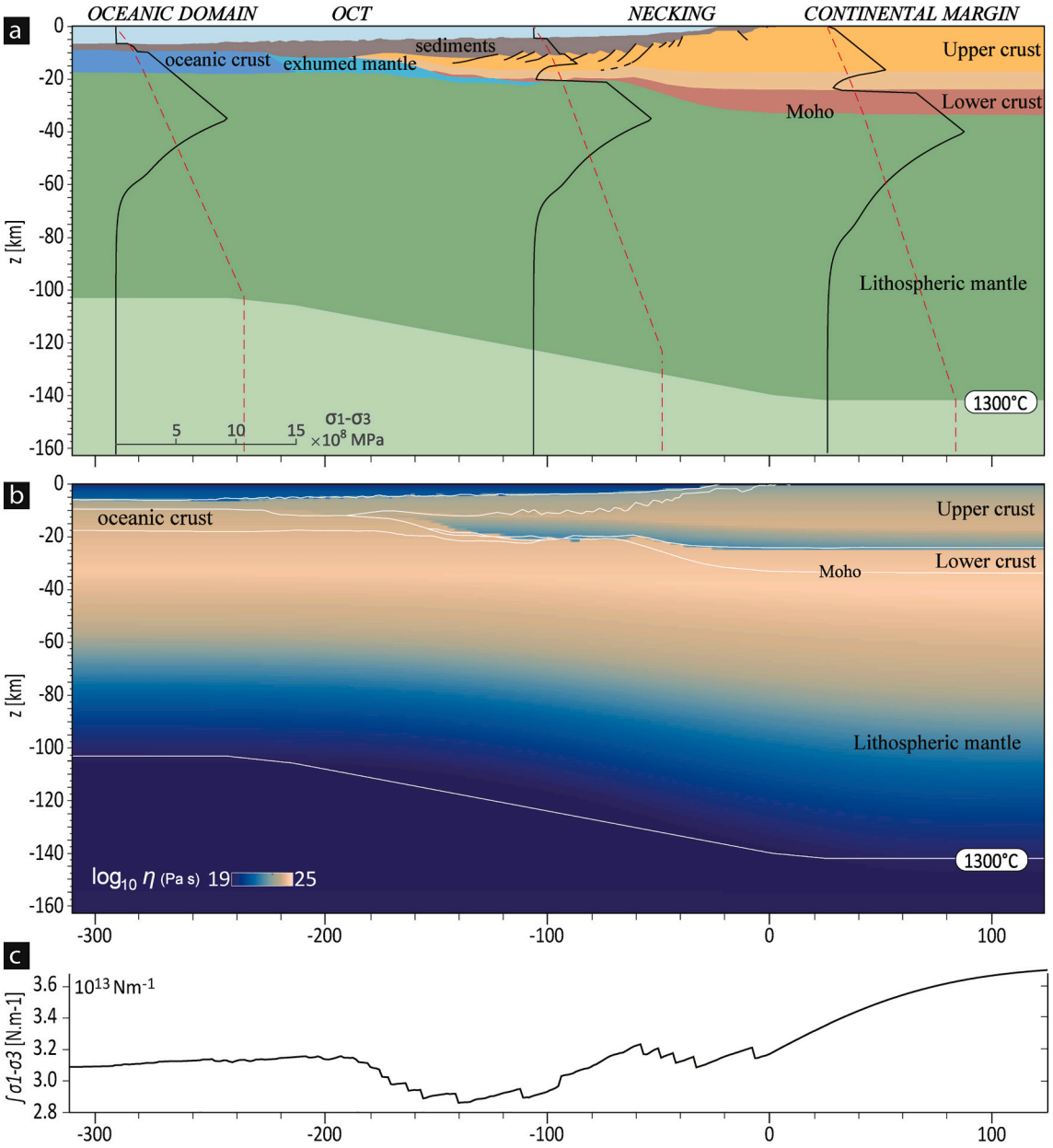

Fig. 1. Overview of geometric and mechanical characteristics of a magma-poor passive margin under compression. a) Interpreted geological cross-section of the Angolan margin (modified after Unternehr et al., 2010) with superimposed strength profiles at key locations b) Effective viscosity obtained using rheological condition displayed in Fig. 1.a. c) Graph representing the integrated strength across the Angolan margin based on the calculated differential stresses shown in Fig. 1a. OCT is ocean-continent transition. The strength envelops are calculated using the finite-difference, marker-in-cell code (MDoodz; Duretz et al., 2016), considering frictional, dislocation, diffusion, and Peierls creep formulations. Details of the numerical modelling used for the calculation are made available in the supporting information. The geotherm is computed assuming steady-state conditions and accounts for different radiogenic heat productions in each layer and a constant asthenosphere temperature of 1330 °C bellow the thermal boundary. Because this boundary is not very well defined in nature, the thermal base of the continental and oceanic lithosphere is kept constant and a linear interpolation is applied between the base of oceanic and continental plate. In accordance with global thermal model of the lithosphere (Artemieva, 2009; Burov, 2011), the depth of the thermal boundary is lower for the oceanic lithosphere.

eventually turn into a subduction zone.

Therefore, we use physical analogue modelling to predict and quantify the deformational and topographic response at passive margins. This allows for shedding light on characteristic length scales of deformation during passive margin inversion and subsequent formation of a new subduction zone. In particular, we seek to obtain new insights in the relationship between the strength of the mantle lithosphere and the locus and style of deformation at passive margins. As such the main variables in this study are the strength of the ductile lithospheric mantle, regulated through changes of mantle viscosity and convergence rate. We demonstrate the relevance of our modelling results by comparison with length-scales of deformation at natural examples.

2. Rheology at passive continental margins

The rheology of passive margins and neighboring oceanic domains can be complex due to significant lateral changes in thickness, composition, structure and temperature of continental and oceanic lithospheres (Fig. 1). Further complexities can be inherited from the geometric and thermo-rheological characteristics of the pre- rift lithosphere, but also from deep thermal and surface processes occurring during the *syn*- and post- rift stages (Buck, 1991; Osmundsen and Redfield, 2011). Regardless their magmatic budget, in general, passive margins are characterized by the wedging out of the continental crust (Fig. 1a and b) over the region where thinning of the continental lithosphere occurred. The width of thinning area varies anywhere from 100 to 600 km (e.g. Osmundsen and Redfield, 2011; Petersen and Schiffer, 2016; Reston and Manatschal, 2011) averaging ~200 km (Bauer et al., 2000). Furthermore, passive margins mark the rheological transition from a single-layer oceanic to a multi-layer continental lithosphere. Depending on rheology and thermal structure, mechanical decoupling may occur between the various layers, such as between the crust and mantle, thereby reducing the overall strength at the margin lithosphere (Burov, 2011). Consequently, the strength of the oceanic crust at passive margins is usually higher than that of the extended continent (e.g., Burov and Diament, 1995; Ziegler and Cloetingh, 2004). As an example, integration of yield-stress-envelopes along a section of a magma-poor passive margin such as the Angolan margin shows a drop in strength at the transition from the oceanic to the continental crust (Fig. 1b). This strength minimum is related to the relatively low lithostatic pressure at the passive margin and low strength of the thinned and extended continental crust at the OCT (Fig. 1a). In the case of the Angolan margin, this low strength region is ca. 40–50 km long. Continent-ward, the thickness of the lithosphere increases, and it becomes stronger than the oceanic lithosphere (Fig. 1b). Although crustal deformation may be enhanced by the strength contrast inherent to the continent-ocean transition, it is not clear how the underlying mantle lithosphere reacts to the applied forces, as failure usually occurs at very high stress levels (Watts and Burov, 2003). Therefore, analogue and numerical simulations frequently implement weak zones or sharp boundaries between different model domains to simulate compositional heterogeneities and localize deformation (Faccenna et al., 1999; Mart et al., 2005; Nikolaeva et al., 2010; Zhong and Li, 2020). The existence of a weak domain may be justified by assuming favourable thermal and compositional conditions. Yet, in nature, heterogeneities are usually more distributed throughout the mantle lithosphere (Maystrenko et al., 2013).

3. Experimental approach

3.1. General concept

Our experiments simulate compression of a magma poor margin as a consequence of far-field forces or forces arising from mid-ocean ridges (Stern, 2004), mantle flow (Baes et al., 2018), gravitational potential energy (Pascal and Cloetingh, 2009), or sedimentary loading (Cloetingh et al., 1984). The model geometry and properties of the materials are displayed in Fig. 2 and in Table 1. Six experiments are shown (Fig. 2b) in which different viscosities of the lithospheric mantle and shortening rates (0.5 and 1 cm/h) applied at model boundaries are used to change the ductile strength of the lithospheric mantle, the main parameter of this study. We thus utilize the stress dependence of viscosity for addressing the effects of different mechanical states of the lithosphere at the onset of deformation. The analogue models were built inside a 36 cm wide, 45 cm long and 15 cm deep tank of transparent Plexiglas (Fig. 2a). They consist of sand (brittle layers) and silicon putties (ductile layers) floating on a low-viscosity fluid that enables isostatic equilibrium throughout the experiments (e.g. Brun, 1999, 2002; Davy and Cobbold, 1991; Dombrádi et al., 2010; Sokoutis et al., 2000, 2005). During the experiment, the model is compressed from one side and confined on all other sides by fixed walls (Fig. 2.2a). Under this condition the model is free to evolve in the vertical direction.

The initial geometric setup consists of an oceanic, a continental and a wedge shape transitional lithosphere in between (Fig. 2a). The latter represents the passive margin, i.e., the necking zone where the continental crust has been thinned most during lithosphere extension. The wedge-shaped domain, separating oceanic from continental lithospheres will be referred to as the “margin”. The length of the model margin scales to a margin length of 150 km in nature, which falls within the range of passive margin lengths (~200 km on average, Bauer et al., 2000). Within this framework, the rheology of the oceanic lithosphere can be approximated by a two-layer system (brittle-ductile) where the brittle-ductile transition (BDT) is located at a depth of ca. 36 km (Burov, 2011). The 70 km thick oceanic lithosphere (scaled to nature) represents the mechanically strong part of a 50–100 *Ma* lithosphere (by using the mechanical base of the lithosphere, e.g. Burov, 2011). In contrast, the continental lithosphere is defined by a four-layer system (brittle-ductile-brittle-ductile) (Burov and Diament, 1995). Key element is the decoupling of the continental crust from the underlying mantle lithosphere along a viscous layer that wedges-out toward the ocean-continent transition (Fig. 2a and c). In the models, the ductile lithospheric mantle layers are homogenous in thickness and composition under both the continental and oceanic crust. As such, we do not impose pre-defined mantle structures in the lithospheric mantle to localize the deformation, such as a weak zone, but use the geological features inherent to the rheological stratification of a passive margin. For the three types of lithosphere used in the models, the brittle thickness is assumed to be constant. Even if a variation in viscosity with a constant brittle-ductile transition depth seems unrealistic, it allows to test buoyancy conditions as function of the strength of the viscous lithospheric mantle (see buoyancy number, section 3.2).

3.2. Materials properties and scaling

Brittle layers exhibiting Mohr-Coulomb behavior are represented by layers of dry feldspar and quartz sand (see Willingshofer et al., 2005 for a detailed description of material properties), whereas mixtures of silicone putty (PDMS and Rhodorsile Gomme-type) with fillers represent ductile layers (see Table 1). All layers were scaled for density. As such, different densities of sand and silicon putty are used to account for the density contrast between the oceanic and continental lithosphere and for a density increase with depth. Density of the ductile layers has been regulated through the addition of quartz sand (experiments 1–4) or barium sulfate (experiments 5 and 6). The viscosity of the asthenosphere is ca. two orders of magnitude lower than that of the mantle lithosphere. After freezing, this facilitates the separation of the lithosphere from the asthenosphere and the sectioning of the model, which is key for gaining insight in the deformational geometries with depth.

The experiments were scaled according to the principles of geometric, dynamic, kinematic and rheological similarity (Hubbert, 1937; Ramberg, 1981; Sokoutis et al., 2000, 2005; Weijermars and Schmeling, 1986). Relevant scaling relationships between the natural prototype and the analogue model were obtained by keeping the average strength of

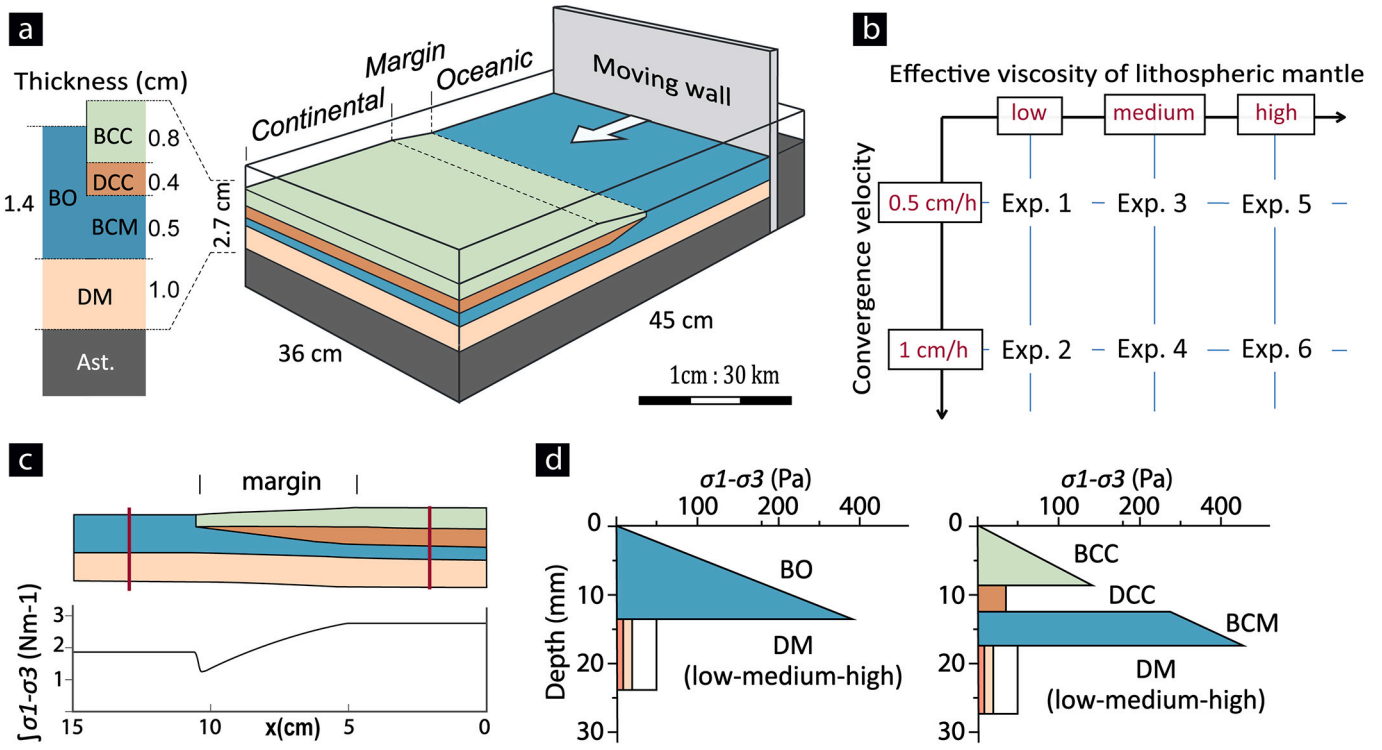

Fig. 2. (a) Experimental setup: four-layer continental lithosphere and a two-layer oceanic lithosphere resting on a high-density, low-viscosity fluid representing the asthenosphere. The white arrow indicates the shortening direction that is applied via the moving wall. BCC, DCC, BCM, DM and BO denote brittle continental crust, ductile continental crust, brittle continental mantle, ductile continental mantle and the brittle part of the oceanic lithosphere, respectively. (b) Matrix showing the parameter space explored in this study. (c) Graph showing computed integrated strength profile under a compressional stress regime for the total lithosphere for models with intermediate viscosity in the lithospheric mantle (LM). (d) Strength profiles for oceanic lithosphere (left) and the continental lithosphere (right) at the onset of deformation. The strength profiles are calculated based on the model geometry as shown in Fig. 2c and on the material parameters given in Table 1. The red lines in Fig. 2c indicate the location of the strength profiles. (For interpretation of the references to colour in this figure legend, the reader is referred to the web version of this article.)

Table 1
Summary of model configurations and material properties per experiment (EXP) together with characteristic properties of natural prototypes. The thickness and density of each layer in the experiments is scaled to nature, based on gravity modelling derived data of different passive margins (Namibian: Bauer et al., 2000; Canadian: Li et al., 2016a; Norwegian: Maystrenko and Scheck-Wenderoth, 2009), and cooling models for oceanic lithosphere (Chapman and Pollack, 1977).

Layers	EXP	Material	Thickness h		Density ρ		Viscosity η		n	F
			Model cm	Nature km	Model kg/ m^3	Nature	Model Pa s	Nature		
Ocean brittle lithosphere		Quartz sand	1.4	42	1500	3350				
Continent brittle crust		Feldspar sand	0.8	24	1300	2900				
Continent ductile crust		Rhodorsil Gomme + sand	0.4	12	1300	2900	4.6e4	4.6e21	1.12	
Continent brittle lithospheric mantle		Quartz sand	0.5	15	1500	3350				
Ductile lithospheric mantle	**Exp1**	Rhodorsil Gomme + sand	1.0	30	1500	3350	1.3e4	1.3e21	1.09	3.03
	Exp2	Rhodorsil Gomme + sand	1.0	30	1500	3350	1.3e4	1.3e21	1.09	1.51
	Exp3	Rhodorsil Gomme + sand	1.0	30	1500	3350	5.8e4	5.8e21	1.13	0.85
	Exp4	Rhodorsil Gomme + sand	1.0	30	1500	3350	5.8e4	5.8e21	1.13	0.42
	Exp5	PDMS + BaSO4+ sand	1.0	30	1500	3350	1.4e5	1.4e22	1.36	0.36
	Exp6	PDMS + BaSO4+ sand	1.0	30	1500	3350	1.4e5	1.4e22	1.36	0.18
Asthenosphere		Polytungstate + glycerol	10	300	1470	3280	~5.0e.2	5.0e19	1.00	

Here h is the thickness, η is the effective viscosity, ρ is the density of the layers and n is the stress exponent. F is the buoyancy number.

the ductile layers correctly scaled with respect to the strength of the brittle layers and the gravity forces (Brun, 1999; Ramberg, 1981). To scale dynamic similarity, we calculate the Reynolds number *Re*, which is a non-dimensional number representing the ratio between inertial forces and viscous forces according to:

$$Re = \rho V h d / \eta \quad (1)$$

where ρ, V, η, hd, are the density, velocity of displacement, effective viscosity, and thickness of the ductile layers. In nature the Reynolds number is generally very small ($Re < 1e^{-20}$) (Dombrádi et al., 2010; Ramberg, 1981; Schellart and Strak, 2016; Sokoutis et al., 2000). In the experiments, $Re << 1$ (e.g. for the ductile lithospheric mantle in exp. 2, $Re = 3.7e\text{-}10$), and therefore, inertial forces can be neglected compared to the viscous ones. This justifies treating the time and length ratios as independent variables (Ramberg, 1981).

The kinematic similarity is satisfied when the model and prototype undergo similar changes of shape or position within a certain amount of time set by the time ratio (t^*), which reflects the duration of deformation in the viscous layer. The time-scale ratio can be calculated using the inverse of the strain rate which is the viscosity ratio divided by the stress

ratio:

$$t^* = \frac{1}{\dot{\varepsilon}^*} = \frac{\eta^*}{\sigma^*} \quad (2)$$

where η^* is the model to nature ratio of the analogue material viscosity to the average viscosity of the natural prototype's ductile layer.

Dynamic similarity for the brittle Mohr-Coulomb-type materials is determined by a dimensionless characteristic stress ratio σ^* which respects the condition $\sigma^* = L^*\rho^*g^*$. (Ramberg, 1981) (*), with ρ, g, L, the density, gravitational acceleration and length respectively and (*) refers to model/prototype ratios (e.g., $L^* = L_m/L_p$). The experiments are geometrically scaled by a length scale factor of $L^* = 3.33\ 10^{-7}$ so that 1 cm in the model corresponds to 30 km in nature. Density is scaled based on the brittle oceanic lithosphere. The stress ratio is then calculated using the density ratio between the quartz sand ($\rho_{qs} = 1500$ kg.m^{-3}) and the mantle lithosphere in nature ($\rho_{oc} = 3350$ kg.m^{-3}), and the length ratio. Then, $\sigma^* = 1.5\ 10^{-7}$.

To respect the friction angle for most crustal rocks $\phi \sim 31°$, dry feldspar and quartz sands with similar friction angles are used in this study (Willingshofer et al., 2005). Then, the maximum differential stress in the brittle layers of the models under compression is given by:

$$(\sigma_1 - \sigma_3)_{\text{Brittle}} = 2\,\rho g z \quad (3)$$

where $\sigma 1$ and $\sigma 3$ are the maximum and minimum principal stresses and z the depth (Brun, 1999, 2002). The slope for the brittle stress is 294.3 Pa/cm representing ~58 MPa/km in nature which is close to Byerlee's law.

To simulate ductile behavior, we use silicone putties with different densities and viscosities (Table 1), which approximate flow by creep (Broerse et al., 2019). Following Jaeger et al. (2009) the differential stress for plane strain can be calculated by using the shear stress (eq. 4). For non-Newtonian materials, shear stress obeys a power law flow law linking stresses to strain rate (or engineering strain rate, $\dot{\gamma}$), and material properties (e.g. Kirby, 1985; Weertman, 1978). The following formulations apply:

$$(\sigma_1 - \sigma_3)_{\text{Ductile}} = 2\tau \quad (4)$$

$$\tau^n = \frac{\dot{\gamma}}{A} \quad (5)$$

$$\dot{\gamma} = \frac{\partial v}{\partial y} \quad (6)$$

where n is the flow behavior index. A is in this case the material viscosity factor for non-Newtonian rheologies obtained from shear tests and (6) expresses shear strain rate as the ratio of velocity (v) over a length scale (y). The exact value of the strain-rate cannot be precisely calculated a priori as it depends on the number and location of faults that develop during model deformation (Midtkandal et al., 2013). For the ductile layers in the analogue experiments, the shear strain rate can be approximated as the ratio between the velocity v applied at the model boundary and the ductile layer thickness h_d.

To respect the strength difference with the brittle layer, the viscosity in nature is used as a proxy. With n values ranging between 1.15 and 1.45, the materials exhibit slightly non-Newtonian behavior. In nature, the effective viscosity of the ductile mantle lithosphere is a function of the strain rate and composition, and typically ranges between 10^{21} and 10^{22} Pa.s (Billen and Hirth, 2005; Bills et al., 1994; Hirth and Kohlstedt, 2003; Kaufmann and Amelung, 2000; Vergnolle et al., 2003; Watts et al., 2013), where low viscosities (~10^{20}–10^{21}) characterize weak mantle lithospheres with fertile composition (Dixon et al., 2004; Chenin et al., 2019; Vergnolle et al., 2003). The viscosity scale ratio was calculated using the time and the stress ratio. The time ratio is constrained through the shear strain rate, assuming a natural shear strain rate in the order of 10^{-14} s^{-1} and a ductile layer thickness of 30 km (in accordance with the analogue model). Solving eq. 6 yields a convergence velocity in nature of 1 cm/yr representing 0.5 cm/h in the experiments. As such an experiment lasting for 20 h represents ~32 Myr of shortening in nature, setting the time ratio (t^*) to 7.20×10^{-11} and the viscosity ratio (η^*) to $\simeq 1.0 \times 10^{-17}$, so that the range of viscosities used in the model (10^4–10^5 Pa s) represents ~10^{21}–10^{22} Pa s in nature.

Following Faccenna et al., 1999, we calculate the buoyancy number (F) to quantify the negative buoyancy force of the oceanic lithosphere relative to the asthenosphere and its relation to resistive forces arising from the viscous lithosphere.

$$F = \frac{\Delta\rho g h_L}{\dot{\gamma}\eta_{lm}} \quad (7)$$

where $\Delta\rho$ is the density contrast between the lithosphere and the asthenosphere, h_L is the total thickness of the lithosphere, η_{lm} is the viscosity of the lithospheric mantle.

A density difference of 30 kg.m^{-3} (representing ~60 kg.m^{-3} in nature) is implemented between the oceanic lithosphere and the underlying asthenosphere to favor gravitational instability at the continent-ocean boundary.

3.3. Surface analysis and quantification of vertical movements

In order to show the spatial and temporal evolution of deformation and associated surface topography, we present our results (e.g. Fig. 3a) in terms of top-view images and cross sections. The latter are obtained at two-third of their width. Experiments are monitored using digital photography and scanning of the top surface. Digital elevation models (DEM's) are calculated from scan data to evaluate the extent of deformation between consecutive time-steps of the experiments (e.g. Fig. 3c). Vertical movements through time are also monitored along profiles to further delineate where deformation takes place. The amplitude of vertical movements was calculated by subtracting the topographic values between two successive time steps. Mean deviations between two successive topographic profiles which are less than 0.1 mm have been filtered out. This threshold was set to eliminate small undulations of the model surface and to focus on the first order topographic response to deformation. The length of the deformation zone (e.g., Fig. 3c) is then defined as the zone where vertical movements from one step to another one are in excess of the threshold. The total sum of vertical movements (TSVM), derived from DEM data, was used to illustrate and quantify regions in the models where most of the deformation occurs during the entire duration of the experiment (e.g. Fig. 3d). TSVM was calculated by adding the values of vertical movements and provides information where in the section vertical movements are dominantly upward or downward.

3.4. Assumptions and simplifications

The experiments aim at simulating the shortening of a thermally equilibrated passive margin lithosphere. Each experiment is carried out with a constant rate of deformation, which is applied through movement of a wall that simulates a horizontal force like ridge push and far field forces. The resolution of the presented analogue experiments accounts for the first-order rheological layering of the lithosphere. The viscous layers of the models are defined by uniform properties over their thickness and absence of temperature dependent variations of the creep strength with depth are included in the model. In contrast, the ductile behavior in natural systems strongly depends on temperature (Brace and Kohlstedt, 1980; Ranalli, 1995). To facilitate setting up of the experiment, materials used in this study have quasi-Newtonian properties ($n = 1$). This deviation from nature ($n = 2$–3) may impede strain localization within the mantle and thus the development of a shear zone, representing the plate boundary. Previous studies demonstrate that representing the ductile behavior of the lower crust and lithospheric mantle with uniform viscous materials is an acceptable first-order

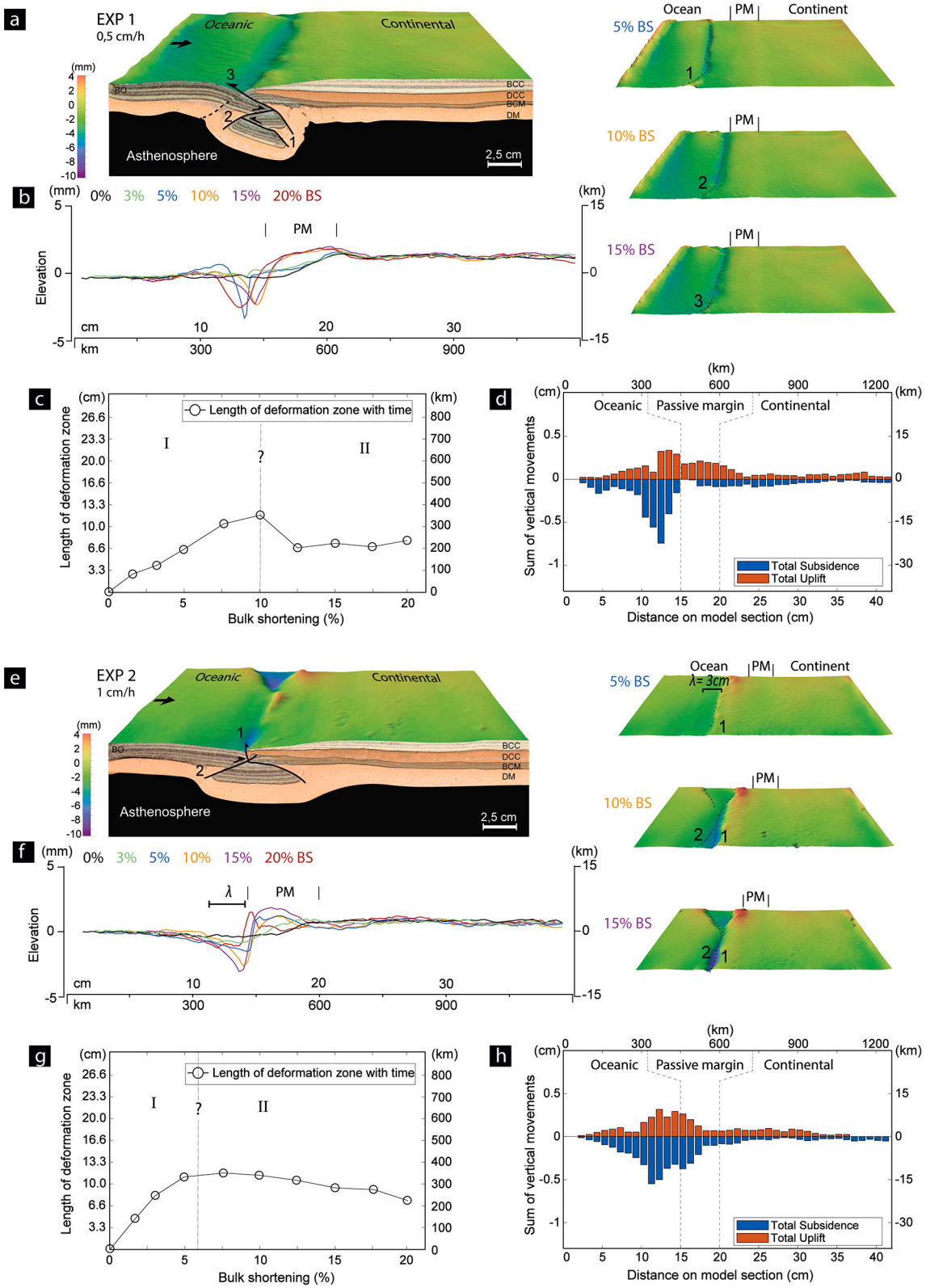

Fig. 3. Results of experiments 1 and 2 testing a weak lithospheric mantle. (a, e) Final, 3D lithospheric scale structure (left) and topographic evolution of experiments (right). The cross-sections are located at two-third of the width from the top of the model. Abbreviations as in Fig. 2. (b, f) Topographic profiles are retrieved through DEMs at 0%, 3%, 5%, 10%, 15%, and 20% bulk shortening (BS). Vertical exaggeration is 10 times. (c, g) Length of the deformation zone at different times of the experiment also expressed in bulk shortening. I, II and III are the three evolutionary stages: (I) inversion of the passive margin (II) unstable under-thrusting and (III) subduction (d, h) Total sum of vertical movements across the section, calculated during the entire time span of the experiment. The amplitude of vertical movement was calculated by subtracting the topographic values between two profiles between two time steps given in the graph in part (c), expressed in bulk shortening. The amplitude of vertical movements was used to define the zone of deformation in part (c, g) and the total sum of vertical movements in part (d, h).

approximation (Chemenda et al., 1996) that does not affect the general results and conclusion (Auzemery et al., 2020; Faccenna et al., 1999; Martinod and Davy, 1992). In nature density contrasts between a mature oceanic lithosphere and the adiabatic mantle range between 20 and 80 $kg.m^{-3}$, (Afonso et al., 2007; Schubert et al., 2001). Following Faccenna et al. (1999), we implement a density difference between the oceanic lithosphere and the underlying asthenosphere, which is 30 $kg.m^{-3}$ in our experiments (representing ~60 $kg.m^{-3}$ in nature) to allow for gravitational instability at the ocean-continent transition. This density contrast is assumed to be constant and the buoyancy is regulated through the strength of the ductile mantle lithosphere. The importance of vertical and lateral density variations for the initiation of subduction zones at passive margins is discussed in detail by Faccenna et al. (1999), Mart et al. (2005) and Maystrenko et al. (2013). The evolution of topography is analyzed without taking into account erosion, transport and deposition of sediments which can be important for the timing of deformation (Malavieille, 2010; Pinto et al., 2010; Willett et al., 1993). The absence of surface processes and the lack of localizing mechanisms in the ductile mantle lithosphere results in exaggerated vertical motions of the model surface. We nevertheless regard the surface scan data as relevant data, which provides critical information on the locus and relative magnitudes of vertical motions.

The kinematic boundary condition (moving wall) creates slight deformation along the sidewalls within a 1–2 cm wide zone. These deformation structures appear at the beginning of the experiments, do not further evolve with time and do not propagate into the interior of the model. As such, they do not bias the modelling results. Despite the simplifications inherent to the analogue modelling technique, the experiments presented here provide first-order deformation patterns and associated topography that characterize the deformational behavior of passive margins under compression.

4. Experimental results

For each rheological setup, two experiments have been performed with different convergence velocities. The results are presented by sets of experiments with weak, medium strength and strong lithospheric mantle. The modelling results are described in terms of three evolutionary stages including: (1) inversion of the passive margin (stage I), (2) unstable underthrusting (stage II) and (3) subduction (stage III). More specifically, stage I refers to the first deformational response to the applied shortening whereas stage II encompasses the switch from distributed to localized deformation. We refer to “subduction” (stage III) when no major changes in deformation width occur and a slab-like feature evolves.

4.1. Weak mantle lithosphere (Set 1)

Experiments 1 and 2 are characterized by a low viscosity lithospheric mantle of 1.7×10^4 Pa s resulting in a buoyancy number that is larger than 1 for both experiments (Table 1), so that stress induced by the negatively buoyant oceanic lithosphere overcomes the ductile resistance of the mantle lithosphere.

Experiment 1 is characterized by a slow convergence velocity of 0.5 cm/h representing ~1 cm/year in nature. Analysis of topographic profiles (Fig. 3b) shows that deformation starts with a very narrow flexure and deformation of the oceanic crust prior to 3% bulk shortening (BS). Deformation results in thrusting within the oceanic lithosphere cutting the model surface parallel to the continent-ocean boundary (Fig. 3a, thrust n° 1). This fault remains active and controls the development of a shallow trench-type basin, which rapidly deepens up to 5% BS (Fig. 3b). During this stage thrusting leads to uplift in the hanging wall, which is limited to the vicinity of the trench (Fig. 3d). In between 5 and 10% BS the thrust polarity reverses and a newly developing thrust (n° 2) displaces thrust n° 1 (Fig. 3a). Thrust polarity reversal leads to the vertical accumulation of brittle material below the ocean-continent transition inducing a widening of the deformed area and uplift of the entire passive margin (Figs. 3b-3d). The subsequent distinct decrease in length of the deformed area is related to a stage where the trench position was stationary and where no additional uplift occurred at the passive margin (Fig. 3b and c, between 10 and 15% BS). Another change of thrusting polarity occurred at ~15% BS (thrust n° 3) without deforming the continental lithosphere. Trench migration toward the ocean is observed at this stage. Vertical motions are mainly localized in the oceanic domain with maximum subsidence at the trench and maximum uplift of the overriding plate in the immediate vicinity of the trench (Fig. 3d). The length of the zone of deformation is relatively narrow and scales to a maximum length of ~350 km in nature (Fig. 3c).

Experiment 2, with a convergence velocity (1 cm/h), evolves similarly to experiment 1. However, the main thrust fault is located much closer to the continental margin. As in experiment 1, the continental margin is not deformed internally, but uplifted in response to thrusting of oceanic crust below the margin (Fig. 3f and h, topographic profile at 5% BS). Prior to underthrusting, a narrow fold with a wavelength of 3 cm marks the flexure of the OCT (Fig. 3e and f, scan and topographic profile at 5% BS). Faster convergence correlates with a more rapid increase in deformation length, but the maximum length of the deformation zone is similar in both cases (Fig. 3g). The trench slowly migrates ocean-ward and gradually deepens during the long-lasting activity of thrust n° 1. The flip in thrust polarity (thrust n° 2) commences at 12% of BS and results in a prismatic pop down bounded by opposite verging thrust faults.

In both experiments, deformation only affects the oceanic lithosphere by the activation of intra-ocean thrust faults. Thrusting is associated with thickening of the crust leading to uplift of the overriding plate and an increase in deformation length. The length of deformation is around 6 to 10 cm in our experiments, representing 200 to 300 km in nature. The maximum width of the experiments (stage I) is reached once the thrust polarity has changed. Thereafter the width of deformation decreased rapidly (experiment 1) and slowly (experiment 2), characterizing stage II in the evolutionary scheme. We note that a stable configuration (stage III) is only achieved in experiment 1. For a buoyancy number larger than one, the viscous resistance of the lithospheric mantle does not prevent the sinking of the crustal blocks. Intra-oceanic deformation is accommodated by major thrusts, which change polarity through time and create large subsidence at trench-type basins. In contrast, the low strength of the lithospheric mantle and its Newtonian behavior results in ductile flow but not in the localization of strain and thus the development of a shear zone at that level.

4.2. Medium strength mantle lithosphere (Set 2)

The second set of two experiments is characterized by an intermediate viscosity of the lithospheric mantle of 5.8×10^4 Pa s and corresponds to passive margins with moderate age and a medium strength lithospheric mantle. The buoyancy numbers for these experiments are 0.85 and 0.43 for the slow and fast experiment, respectively.

Experiment 3 with a slow convergence velocity of 0.5 cm/h shows deformation of the passive margin and almost no deformation in the oceanic domain (Figs. 4a-4d). Shortening results in deformation of the OCT commencing after 5% BS (Fig. 4a, fault 1 and 2). Coevally, the former passive margin is flexed downward at a wavelength of 11 cm (Fig. 4a, scan at 5% BS). This flexural basin is flanked on both sides by bulges. We note that deformation spreads over a wide area covering the entire margin at this early stage (stage I) in model evolution (Fig. 4c). Thrusting localizes where the ductile lower crust of the margin wedges-out and develops with a backward sequence in the direction of the continent. A trench-type basin forms between the oceanic and the continental lithospheres, and progressively deepens during shortening, as illustrated by the topographic profiles at 5% BS. After 10% BS, the down-flexed passive margin is cut by the evolving fault 2 (Fig. 4a) and underthrusts the continent. This step probably marks the starting of the

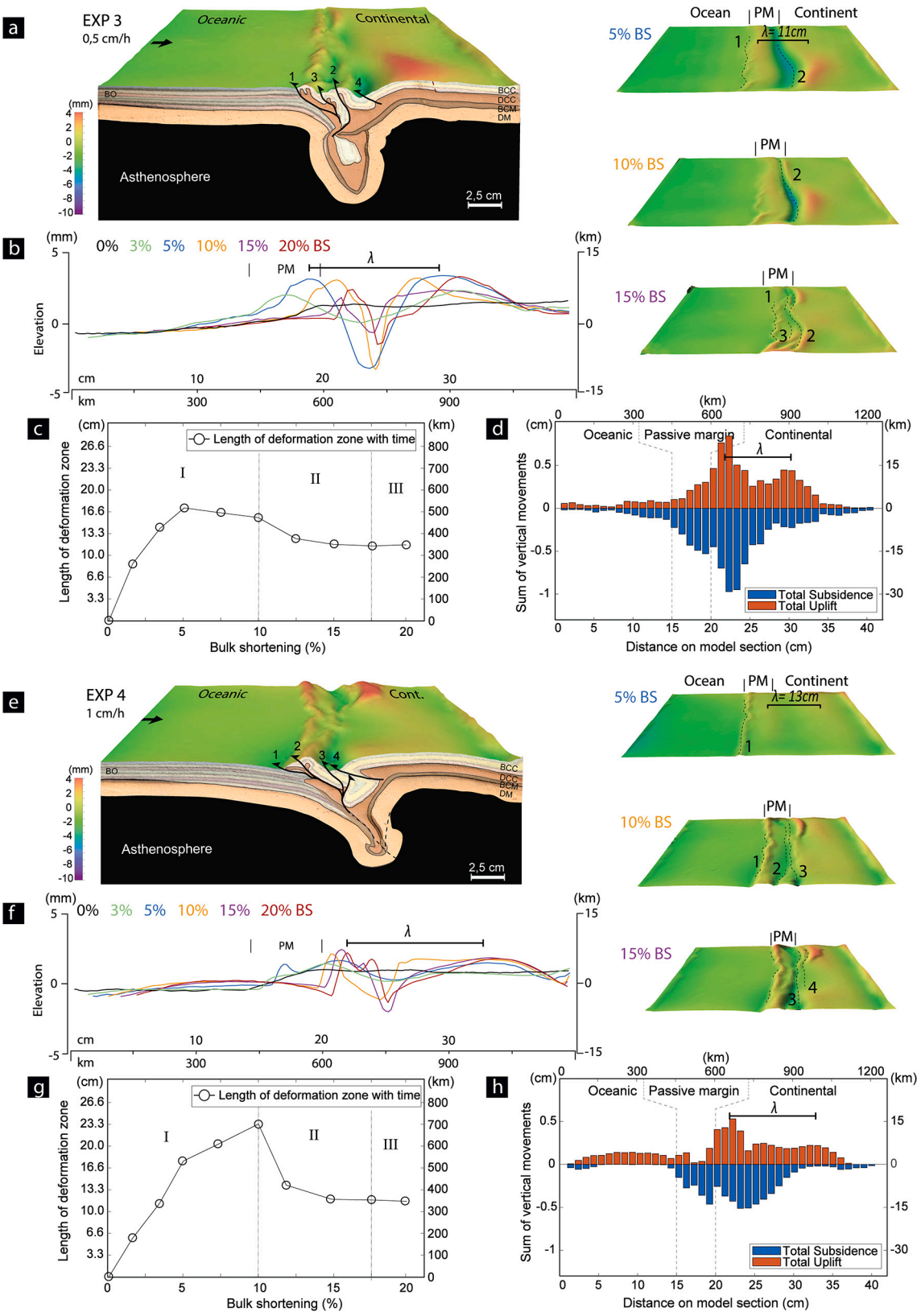

Fig. 4. Results of Experiments 3 and 4 testing a moderate viscosity of the lithospheric mantle. For explanation of the figure, see Fig. 3.

underthrusting stage (stage II) where deformation is mainly localized at the passive margin. It is characterized by a decrease in length of the zone of deformation (Fig. 4c, between 10% and 17%BS). At this stage, the displacement of the deformed margin toward the continent and the stationary character of the continental edge suggests that the continental crust at the margin gets squeezed by the oceanic lithosphere. The cross-section shows that the whole passive margin is accreted at the trench and the down-going plate drags part of it. In particular the accreted

brittle crust is decoupled from the underlying mantle at the level of the ductile lower crust. The cross section at the end of the experiment displays the geometry of a vertical slab-like feature, formed during stage III.

Experiment 4 with a convergence velocity of 1 cm/h resulted in a similar sequence of events and deformation pattern although the topography is lower than in experiment 3. Deformation at the ocean-margin transition creates more scattered vertical movements and induces rapid uplift at the continental side. Development of a thrust system results in a rapid increase of the length of the deformed area (Fig. 4g). Coevally the continental lithospheric mantle is shortened and folded with a wavelength of 13 cm, leading to an uplift of 3 mm. A shallow flexural basin formed behind the thrust-system at the margin and rapidly closed, after 10% BS. During this stage the length of the zone of deformation increases (Fig. 4g, 0–10% BS). However, when the trench is formed and underthrusting starts (stage II), deformation localized at the trench, and the length of deformation decreases (Fig. 4g, 10–17% BS). The almost stationary character of the trench and of the continental edge suggest that underthrusting is mainly controlled by the

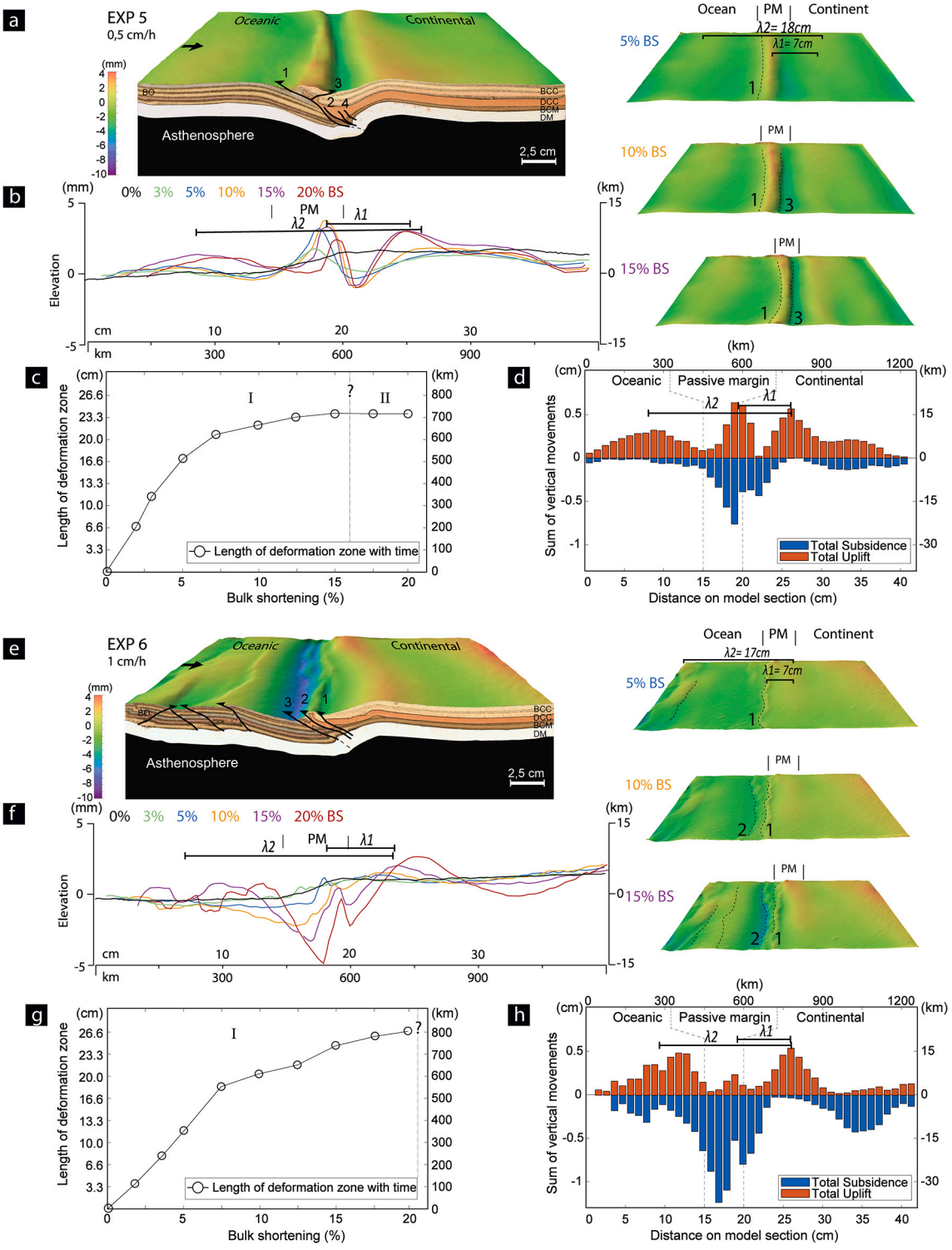

Fig. 5. Results of Experiment 5 and 6 testing a strong lithospheric mantle. For explanation of the figure, see Fig. 3.

convergence of the oceanic plate. Underthrusting is again facilitated by decoupling above the Moho and also drags down the continental mantle lithosphere, which together with the oceanic mantle lithosphere envelopes a tight syncline cored by ductile lower crust. We interpret the constant length of deformation during the last stage of the experiment (Fig. 4g, 17% BS) as marking the final phases of deformation (stage III).

In both experiments, thrusts strike parallel to the evolving trench. The mechanically weak lower continental crust controls the locus of thrust formation and acts as a decollement in which the upper crustal thrusts root. The ductile lower crust allows for crust-mantle decoupling, ultimately leading to partial delamination of the mantle lithosphere. The two experiments differ at this stage such that exp. 4 shows a clear delamination expressed by the strong deformation of the lower crust whereas exp. 3 shows more or less lithospheric dripping. In both experiments, deformation mainly affects the passive margin and is associated with the formation of a flexural basin between oceanic and continental lithosphere over a length of ca. 500–600 km when scaled to nature. Localization of deformation at the passive margin and at the continental edge, induces strong vertical movements (Fig. 4g and h). Uplift increases progressively during underthrusting. It is caused by the accretion of material at the trench and short wavelength ($\sim\lambda = 300$ km, scaled value) buckling of the continental crust (anticline between 22 and 32 cm on the topographic profile). The experiments also show that the topographic response depends on the convergence rate, creating longer but lower amplitude folding for high convergence rate. The switch from widespread deformation during the early evolution of the experiments (stage I) to localized underthrusting (stage II) is characterized by a reduction in length of the deformation zone amounting to ca. 300–400 km (Figs. 3.4c, g). In both cases, stage III is characterized by a constant length of deformation.

4.3. Strong mantle lithosphere (Set 3)

A lithospheric mantle with a viscosity of 1.4×10^5 Pa s characterizes the third set of two experiments representing passive margins with a strong lithospheric mantle. The buoyancy number for these experiments is 0.36 and 0.18 for the slow and fast experiment respectively.

Experiment 5 corresponds to a slow convergence velocity of 0.5 cm/h. Up to 5% BS deformation is marked by the development of a frontal thrust (n° 1, Fig. 5a), located at the boundary between oceanic lithosphere and passive margin. This thrust induces short wavelength crustal folding ($\lambda 1 \sim 7$ cm wavelength). Coevally, downward flexure of the margin defines a basin at the backlimb of the thrust. At 5% BS, the margin is subject to long wavelength folding $\lambda 2$ (18 cm wavelength) and uplift up to 4 mm (see scan and topographic profiles, Fig. 5b). The length of the zone of deformation gradually increased (Fig. 5c). During thrust propagation, a strong uplift affects the basin edge in response to flexure. At 20% BS, the section reveals that the main thrusts (n° 1 & 2) cut through the brittle mantle layer. However, these faults do not propagate through the ductile lithospheric mantle. Strong ductile resistance of the mantle lithosphere opposes the slab descent and folding affects the entire lithosphere as shown by the cross-section.

Experiment 6 corresponds to a fast convergence velocity of 1 cm/h. This experiment shows a geometrical pattern comparable to experiment 5 but with the different stages developing simultaneously. Underthrusting of the oceanic plate does not occur and shortening is accommodated by short wavelength crustal folding ($\lambda 1 \sim 7$ cm) and large wavelength lithosphere buckling of both the continent and the ocean ($\lambda 2 \sim 17$ cm, profile Fig. 5f). Similar to experiment 5, the passive margin subsides, and the continental edge is uplifted (Fig. 5). In addition, folding is associated with low-offset, dominant oceanward-verging thrusts and pop-up structures. High topography reveals that deformation amplitude is large in the oceanic domain and decreases at the OCT and in the continental lithosphere close to the trench. Flexure is more pronounced than in experiment 5 and affects the trench, the frontal thrust system and the fore-arc basin.

In both experiments the failure of the crust occurs at the OCT. At high shortening velocity, deformation is distributed over a wider area expressed by regions of uplift and subsidence (Figs. 5b, f, d & h). The highest topography is observed at the continental edge. Although the cross-section of experiment 5 suggests that underthrusting (stage II) occurs, none of the experiments is characterized by a reduction in deformation width. Instead, the area affected by deformation reaches a steady state (experiment 5) or continuously increases (experiment 6), indicating that shortening is dominantly accommodated by long-wavelength folding ($\sim\lambda = 500$ km, scaled value) controlled by the high strength of the ductile mantle lithosphere. The zone of deformation represents 700–800 km in nature. The combination of near surface brittle deformation and lithosphere folding gives rise to a very pronounced and characteristic topography development (Figs. 5d). As a consequence, the continental margin edge experiences a strong uplift whereas the foreland is marked by a pronounced subsidence. As in previous experiments, the transition between oceanic and passive margin lithosphere shows local uplift caused by the deformation of the thinned crust and its accretion.

5. Discussion

5.1. Strain localization

Our experimental results consistently highlight the dependence of strain localization and locus of deformation on the viscosity of the ductile lithospheric mantle and thus its strength, despite the lateral homogenous nature of the ductile mantle lithosphere. For the effect of lateral strength variations in the lithospheric mantle the reader is referred to Calignano et al. (2015) or Santimano and Pysklywec (2020). The rheology of the mantle lithosphere has a strong effect on the distribution of deformation, such that deformation localizes within the oceanic lithosphere with a low strength mantle layer, whereas it localizes at the OCT in all other cases (lithospheres with intermediate and high ductile mantle viscosity, Figs. 4 and 5). Additionally, increasing the viscosity of the mantle lithosphere also leads to a change in deformational behavior within that layer from thrust dominated (experiments 1–4) to folding dominated (experiments 4–5). As in all experiments the oceanic and continental crust remained unchanged, we argue that the above-mentioned differences are a direct consequence of differences in shear resistance in the ductile mantle lithosphere, a parameter that is key for developing shear instabilities which potentially evolve into subduction zones, as shown by previous analogue modelling studies (e.g. Faccenna et al., 1999; Goren et al., 2008; Luth et al., 2010; Sokoutis and Willingshofer, 2011; Willingshofer et al., 2013).

Although incipient deformation is more easily achieved within the passive margin crust because only low stress levels are required to mobilize the ductile layer, the stability of the lithospheric mantle is critical for the further evolution of the system. Previous analogue modelling studies have shown that the negative buoyancy of the oceanic plate as well as the density contrasts between continental and oceanic lithospheres are important for passive margin inversion and in particular for subsequent subduction initiation (Chemenda et al., 1996; Faccenna et al., 1999; Goren et al., 2008; Leroy et al., 2004; Mart et al., 2005). Following Faccenna et al. (1999), we use the buoyancy number (Fig. 6a) to characterize system behavior. In addition, our experiments show a relationship of F to the place where deformation initiates. If $F > 1$, the stability of the oceanic lithosphere here is compromised, and underthrusting occurs in the oceanic domain (experiments 1–2). These modelling results apply for cases of high negative buoyancy of the oceanic lithosphere which seems to be at variance with the low viscosity in the lithospheric mantle (less than $2\ 10^{21}$ Pa s in this study). As viscous strength in nature increases rapidly with age (England and Wortel, 1980), intra-oceanic lithosphere instability requires large negative buoyancy and large melt flux through the lithosphere to facilitate its weakening. A suitable natural example would be the inversion of a

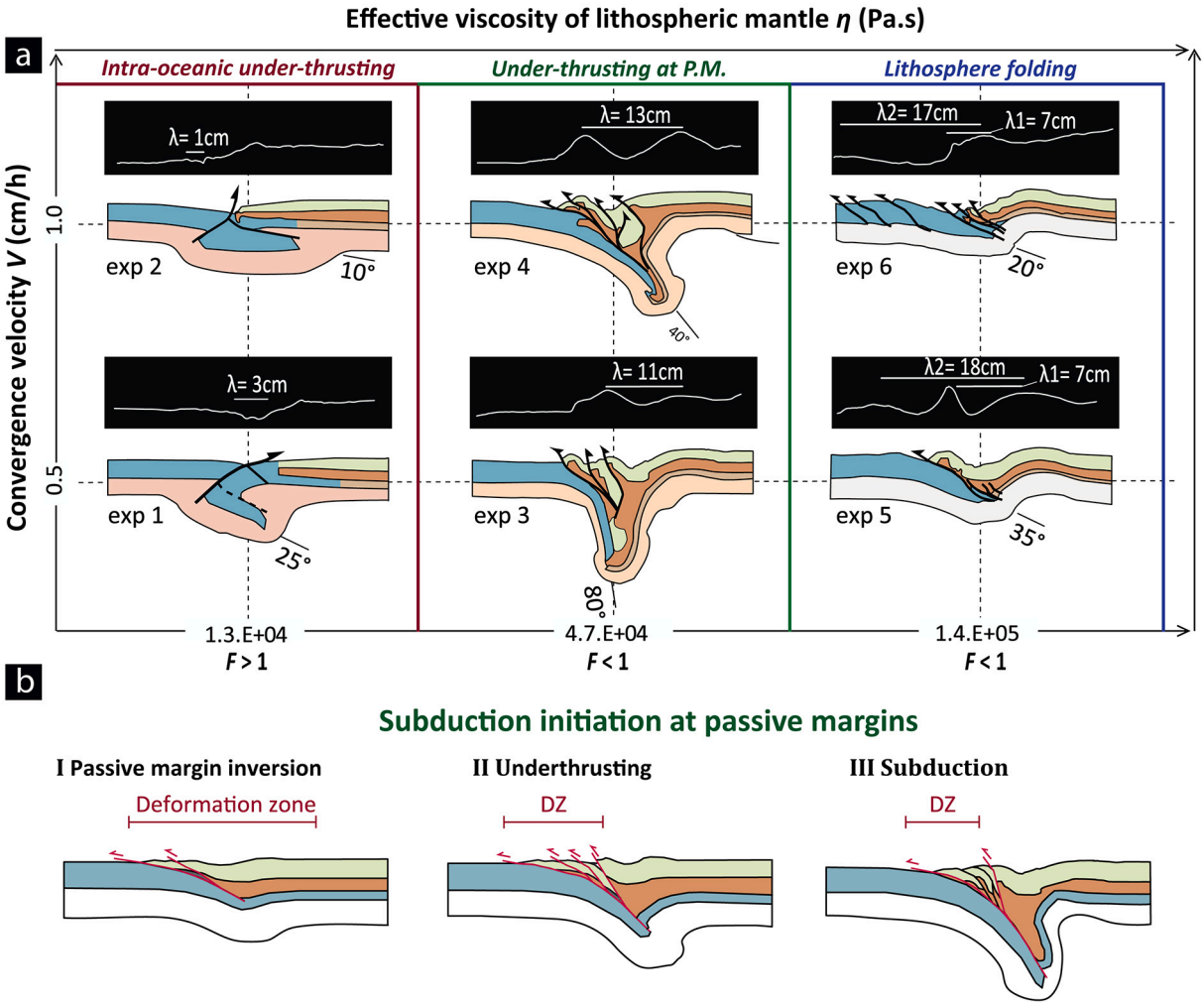

Fig. 6. (a) Summary of modelling results for tested parameters of this study. (b) Mode of deformation at passive margins including I passive margin inversion, II unstable under-thrusting, and III subduction. Red segments represent the length of the deformed region. The figure shows a schematic illustration of the evolution of deformation at a passive margin with favourable conditions for subsequent subduction initiation. (For interpretation of the references to colour in this figure legend, the reader is referred to the web version of this article.)

partially melted oceanic lithosphere by subduction-induced mantle upwelling (Strak and Schellart, 2018) or a mantle plume setting (Burov and Cloetingh, 2010; Gerya et al., 2015; Monnereau et al., 1993; Rolland et al., 2009). The latter might well have been the case for Caribbean subduction initiation (Whattam and Stern, 2015).

In the case of a stable lithosphere ($F < 1$), deformation occurs at passive margins. In general, a low buoyancy number should prohibit underthrusting (Faccenna et al., 1999). However, adding a contractional component of deformation seems to allow for deviating from this concept and facilitates underthrusting even with buoyancy numbers as low as 0.8 or 0.4 (experiments 3 and 4). To find explanations for this apparent discrepancy the pre-underthrusting stage of deformation needs to be considered. Detailed analysis of the deformational sequence revealed that early stages of deformation that predominantly affected the passive margin (experiments 3 & 4) are characterized by thrusting, which commences at the tip of ductile continental crust, where horizontal shortening is accommodated by layer-parallel shear. This is illustrated by the presence of ductile material along the ramp of the oldest thrust, number 1 (Fig. 4a and e). As such we suggest that the rheological stratification of the passive margin and in particular that of the ductile crust provides a first order control on the locus of deformation during incipient margin inversion (stage I). Similar to Nikolaeva et al. (2011), our experiments suggest that the early stage deformation in the crust pre-conditions where deformation will be transferred to the mantle lithosphere. More specifically, shear localization and associated deformation at the base of the continental crust regulates the degree of coupling and permits deflection of the oceanic plate under the margin (Fig. 6b), thereby creating a mechanical instability allowing for the change of distributed deformation (stage I) to localized deformation (stage II) and ultimately for partial delamination of the mantle lithosphere. When deformation localizes at the base of the crust, the strength of the mantle lithosphere controls the extend of underthrusting and thus the stability of the margin. These results are consistent with earlier analogue modelling studies that emphasize the importance of decoupling horizons for the localization and geometry of deformation in convergent settings (e.g. Willingshofer and Sokoutis, 2009).

We note that the convergence velocity plays also an important role in the delamination process. Therefore, favourable conditions for inversion of passive margins that might evolve into a subduction zone lie in a limited spectrum of lithospheric mantle viscosities of around 5.0 10^{21} Pa s (when scaled to nature), which is consistent with intermediate to mature oceanic lithospheres (Auzemery et al., 2020; Oxburgh and Turcotte, 1976; Turcotte and Schubert, 2014), or again a thermally weakened lithosphere at the margin (Jammes and Lavier, 2016). For viscosities higher than that shortening will lead to large-scale folding of the margin and neighboring lithospheres (Fig. 6a). In the extreme case, lithosphere folding and associated thrusting can affect oceanic plates as observed in the Indian ocean (Beekman et al., 1996; Stein et al., 1989a).

This strong type of lithosphere produces deformation at crustal levels equivalent to experiment 5 and 6. We acknowledge that thermal inputs could change these conditions and could impact on margin evolution.

5.2. Comparison with numerical modelling

The analogue models display striking similarities with numerical models of passive margin inversion and in particular of subduction initiation (e.g. Nikolaeva et al., 2011; Kiss et al., 2020). Both methods highlight the role of the strength of the mantle lithosphere and of crust/mantle decoupling at passive margins. However, the quasi-Newtonian viscosities in the analogue experiments impede strain localization within the mantle and thus the development of a shear zone, representing the plate boundary, which would then accommodate the downward motion of the subducting plate (Fig. 6b, III). Instead, downward motion involved both, the subducting as well as the overriding plate (Fig. 6b, III) leading to "two-sided"subduction as described by Gerya et al. (2008). In our models, this behavior can be attributed to the lack of externally imposed or intrinsic weakening mechanisms such as shear heating (Auzemery et al., 2020; Kiss et al., 2020; Thielmann and Kaus, 2012) or fluid percolation (Alvarez-Marron et al., 1997; Regenauer-Lieb et al., 2001), respectively. Based on our experimental results, we argue that in the absence of inherited weak zones or weakening mechanism, incipient subduction should be two-sided until one of the above-named processes or a combination thereof leads to strain localization. In this case, subduction can also involve part of the continental lithosphere such as in experiment 3.

Additionally, thermo-compositional mechanisms may contribute to

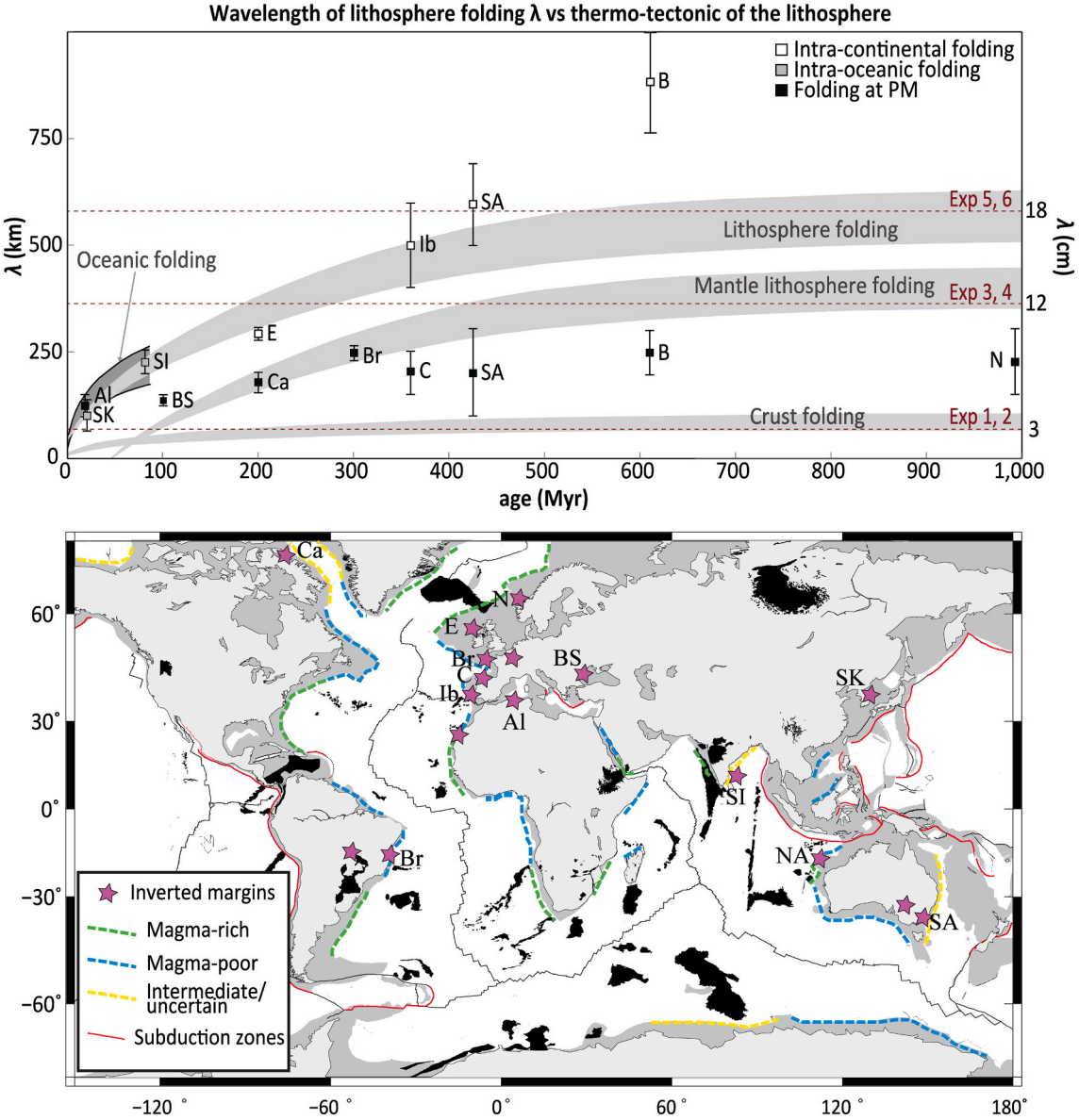

Fig. 7. Relationship between wavelengths of lithospheric folding and thermo-tectonic age of lithospheres in nature (modified after Cloetingh and Burov, 2011, references in Table 2), corresponding to the age of formation of the continental plate, and including data for Algeria (A), Northern Australia (NA), Southern Australia (SA), Black-Sea (BS), Brazil (B), Canada (Ca), Cantabria (c), Europe (E), Iberia (Ib), Southern India(SI), Norway (N), South-Korea (SK) passive margins. (Top) Theoretical folding wavelengths, derived from analytical models, for continental lithosphere (Cloetingh et al., 1999) as well as for oceanic lithosphere (McAdoo and Sandwell, 1985). The red dashed line is the folding wavelength as deduced from the analogue modelling. (Bottom) Map showing the distribution of major passive continental margin types (modified after (Reston, 2009), and the locations of tectonically inverted passive margins during the Cenozoic (magenta stars). Continental shelves (dark grey shading) and plate boundaries (thin lines) are from Müller et al. (2008). Black areas correspond to large igneous provinces. (For interpretation of the references to colour in this figure legend, the reader is referred to the web version of this article.)

the stability of the mantle lithosphere as shown by Boonma et al. (2019) to explain the variation in strength in the mantle lithosphere. Convergence rate, which regulates thermo-compositional mechanisms may be of particular importance in nature to create instabilities at depth > 140 km (Boonma et al., 2019). Moreover density-enhancing processes, like eclogitization, should occur in the under-thrusted lithosphere, such that slab pull may start after 100–150 km of forced underthrusting (Gurnis et al., 2004; Maffione et al., 2015). At this depth partial melting might also have a strong effect on the strength of the lithosphere. Nevertheless, at depth shallower than 150 km, other mechanisms are required to explain instability at a passive margin, and we assert that a relatively weak mantle lithosphere is a condition.

5.3. Length scales of deformation during passive margin inversion

Similar to our experiments, inverted passive margins are marked by local deflection at the OCT (e.g. Hamai et al., 2015), increased seismicity/deformation at the margin (Stein et al., 1989b), strong uplift of the continental edge (Leroy et al., 2004) and folding of the continental lithosphere (Cloetingh et al., 1999; Ziegler et al., 1995). Moreover, our experimental results consistently show the dependence of length scales of deformation on the strength of the ductile lithospheric mantle (Fig. 6a). Low viscosity of the ductile mantle lithosphere results in localized intra-oceanic deformation whereas stronger mantle lithospheres lead to wide deformation of the passive margin. In particular, prior to underthrusting, the passive margins are marked by folding where the wavelength is controlled by the strength of the mantle lithosphere. Converting the periodicity of the folds in models to the natural scale, the associated length-scales of folding are in the order of 50 to 90 km for experiments with a weak mantle lithosphere, 350–400 km for experiments with medium lithospheric mantle viscosities and 600–700 km for experiments with a strong mantle lithosphere (Fig. 7). Therefore, our experimental results are consistent with the findings of Cloetingh et al. (1999), suggesting that lithospheric folding is a primary response of the lithosphere to shortening. Moreover, Cloetingh and Burov (2011) emphasize the dependence of fold wavelength on plate age and thus strength of the mantle lithosphere. Along these lines we compare our experiments with estimates of folding wavelengths from oceanic and continental lithospheres as well as margins with different thermo-mechanical age (Fig. 7 and Table 2).

In our experiments, shortening of lithosphere with a weak mantle layer results in very localized deformation in the weaker oceanic plate and a very gentle deflection at the margin (exp.2). In nature, contraction of a young lithosphere, such as present at the Algerian or the South-Korean margin, gives rise to localized deformation at the OCT, that includes downward bending of the oceanic plate relative to the continental crust (Hamai et al., 2015) and development of short wavelength folds (70–100 km) in the oceanic domain (Kim et al., 2018). Moreover, the Algerian margin also reveals high seismicity at the OCT (Fig. 8a). However, there is little evidence for on-going deformation further onshore. By comparison, our experimental results suggest that a weak oceanic lithosphere accommodates most of the shortening and deformation of the passive margin is expressed by its deflection. As such we argue that deformation of a very young passive margin (Kim et al., 2018; Hamai et al., 2018) does not necessarily provide evidence for underthrusting at the margin (Fig. 8d).

Length-scales of deformation deduced from experiments 3–4 are consistent with deformation of a decoupled continental lithosphere (Fig. 8 h). In nature, the wavelength of folding of inverted passive margins plots somewhat lower compared to theoretical predictions of folding wavelengths from Cloetingh et al. (1999) (Fig. 7), suggesting that the thermo-tectonic age of the margin lithosphere is lower because of thermal inputs during rifting. This is, for example, the case for the passive margins of the Black Sea (Cloetingh et al., 2008; Starostenko et al., 2013), Arctic Canada (Stephenson and Cloetingh, 1991), Brittany (Bonnet et al., 2000), Norway (Løseth and Henriksen, 2005; Pascal and Cloetingh, 2009), or northern and southern Australia (Holford et al., 2011; Keep and Harrowfield, 2008; Quigley et al., 2010). These margins show local deflections at the OCT, uplift at the margin and the development of a continental flexural basins with a wavelength of 100–300 km (Fig. 7). Among them, the Cantabrian margin is probably the best example of margin inversion prior to underthrusting (De Vicente and Vegas, 2009). The Cantabrian domain is the western continuation of the Pyrenees and reflect inversion of the North-Iberian margin during the Eocene-Oligocene rather than a continental collision. The gravity data of the margin show a gentle gradient in gravity anomaly toward the south (Fig. 8f, Pedreira et al., 2007, Teixell et al., 2018) typical of plate flexure (Karner and Watts, 1983). Additionally, a thrust system is convincingly imaged at the OCT associated with an Eocene-Oligocene wedge (Fig. 8 g). Further south, Eocene *syn*-compressional sediments are identified on the hinterland marginal basin while the margin shoulder is uplifting. All these observations point toward the development of a thrust system at the OCT during Eocene time, which induces a gentle flexure at the margin ($\lambda \sim 250$ km). Further shortening probably would have led to underthrusting as predicted by our models. In the Cantabrian domain, however, underthrusting occurred toward the ocean, giving rise to early stage continental subduction or delamination (Teixell et al., 2018). In contrast to models 3 and 4, lithospheres with a strong mantle lithosphere do not evolve into subduction zones and are characterized by long wavelength lithosphere-scale folding (exp. 5 and 6, Fig. 5). These experiments are in agreement with offshore and onshore observations of old and/or strong passive margin lithospheres such as present at the south Brazilian margin and the north Atlantic margin. The late Cenozoic exhumation episodes identified in the British Isles and adjacent regions were most likely caused by the transmission of compressional stresses into continental NW Europe from the Mid-Atlantic Ridge and the Alpine orogen (Holford et al., 2009; Ziegler et al., 1995). Deformation is identified across long distances exceeding 1000 km and includes different styles such as reactivation and inversion of pre-existing faults (Lundin and Doré, 2002), uplift at the margin (Holford et al., 2009) and

Table 2
Wavelengths and thermo-tectonic ages of folded lithosphere displayed in Fig. 7.

Id	Area	Ages of lithosphere (Myr)	Folding wavelengths λ (km)	References
Al	Algerian margin	16–25	100–150	Hamai et al., 2015; Roure et al., 2012
NA	Northern Australian margin	540–560	200–300	Keep and Harrowfield, 2008
SA	Southern Australia intra-continental	390–450	500–700	Holford et al., 2011; Célérier et al., 2005
SA	South Australian margin	390–450	100–300	Quigley et al., 2010;
BS	Black-Sea margin	75–125	125–150	Cloetingh et al., 2008 Starostenko et al., 2013
B	Brazil Intra-continental	590–630	750–1000	de Lima, 2000
B	Brazilian margin	590–630	200–300	This study
Br	Brittany margin	210–290	225–275	Bonnet et al., 2000
Ca	Canadian (Arctic) margin	150–250	150–200	Stephenson and Cloetingh, 1991
C	Cantabrian margin	330–370	150–250	This study; Viejo and Gallastegui, 2005
E	Western Europe	180–230	270–300	Ziegler et al., 1995; Holford et al., 2009
SI	South Indian margin	80	200–250	Beekman et al., 1996
Ib	Iberia intra-continental	330–370	400–600	De Vicente and Vegas, 2009
SK	South-Korea	20–25	70–100	Kim et al., 2018
N	Norway	1000	100–300	Løseth and Henriksen, 2005

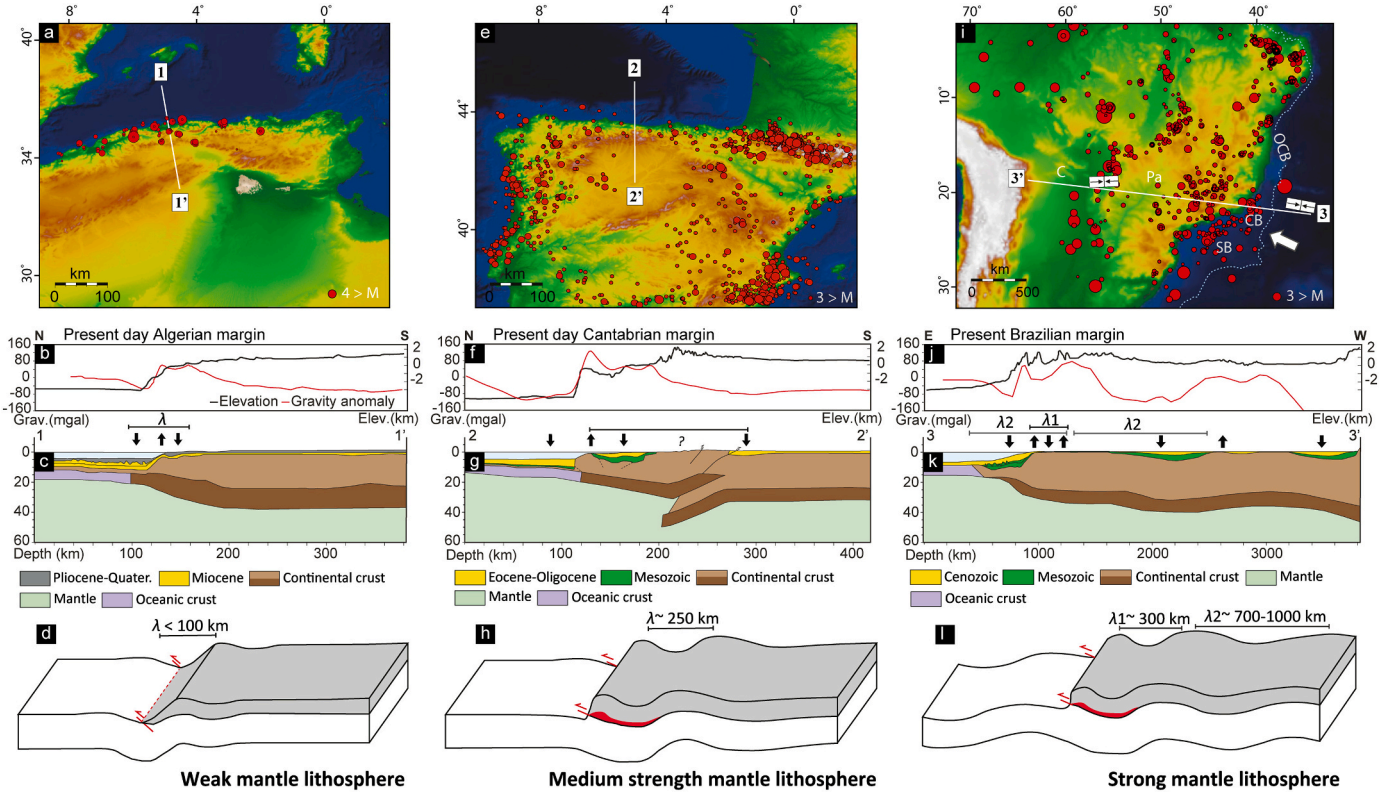

Fig. 8. (a, e, i) Relief map (NASA Worldview) with epicenters of crustal earthquakes (red dots). Campos Basin (CB), Chaco basin (C), Santos Basin (SB), Parana basin (Pa), Ocean Continent Boundary (OCB). (b, f, j) Measured free air gravity anomalies (red line) and topography (black line) for the Algerian margin (Leprêtre et al., 2013), Cantabrian (Viejo and Gallastegui, 2005) and Brazilian (Van der Meijde et al., 2013) margins, respectively. (c, g, k) Crustal models of the passive margins indicating length-scales of deformation: (λ/λ1) short and (λ2) long wavelength folding as a function of mantle lithosphere strength. The compilations are based on: the Algerian margin: (Benhenni et al., 2019; Hamai et al., 2015; Leprêtre et al., 2013); the Cantabrian margin: (Teixell et al., 2018; Viejo and Gallastegui, 2005), the Brazilian margin: (Chulick et al., 2013; Milani and Zalán, 1998; Stanton et al., 2019). (d, h, l) Cartoons showing wavelength of deformation as function of mantle lithosphere strength. The red layer shows the decoupling of deformation at the passive margin.

long-wavelength buckling of the European lithosphere (Bourgeois et al., 2007; Holford et al., 2009; Ziegler et al., 1995). Similarly, the South American Plate is experiencing horizontal compression and shortening controlled by Andean tectonics and compressional interaction of the continental lithosphere with the strong oceanic lithosphere found eastward (de Lima, 2000). Along the Brazilian margin, the offshore earthquakes distributed along the continental shelf and slope are predominantly due to reverse faulting (Assumpção and Sacek, 2013). There, the edge of the continental margin records Neogene-Pleistocene fault inversion (Cogné et al., 2012; Riccomini et al., 2004) and strong uplift in the Campos do Jordão plateau (Modenesi-Gauttieri et al., 2011) and the Taubaté Basin (Cogné et al., 2012). In the same area, several studies show that the direction of the maximum horizontal stress trends *E*-W (Assumpcao, 1992; Barros et al., 2009; Chimpliganond et al., 2010; Coblentz and Richardson, 1996; Ferreira et al., 1998; Neto et al., 2013). Further onshore, a similar compressional E-W trend is observed in the Parana, Pantana and Chaco basins (Milani and Zalán, 1998; Rocha et al., 2016; Ussami et al., 1999). The presented analysis of the south American plate accounts for ongoing deformation including short wavelength lithosphere folding at the margin $\lambda/\lambda 1$ that is ca. 300 km long, typical of a mantle lithosphere folding (Fig. 7), associated with long wavelength antiforms $\lambda 2$ of the order of 750–1000 km (de Lima, 2000), representing whole lithosphere folding. Assuming that the majority of the data are indeed related to inversion, it is unlikely that these margins are evolving into subduction zones.

The above quoted observations constrain a zone of deformation as function of mantle lithosphere strength. We propose three modes of inversion for passive margins under-compression: (1) Compression of weak oceanic lithospheres at continental margins leads to localized deformation in oceanic domain and very short wavelength deflection at the OCT (ca. 50–100 km) (Fig. 8d). (2) Compression of a stronger oceanic lithospheres at continental margins leads to flexure at the OCT, uplift at the margin followed by folding of the continental lithosphere over a distance of λ = 100–300 km (Fig. 8 h). This type of margin represents the best candidate for subduction initiation and a deformational sequence from folding to underthrusting is expected. (3) Compression of strong/old margin lithosphere leads to short wavelength folding at the margin (ca. $\lambda 1$ = 300 km) and long wavelength lithosphere buckling ($\lambda 2$ = 500–1000 km) in oceanic or continental domains, with very little chance of subduction (Fig. 8 l). Comparison with analytical models shows that the wavelength of folding $\lambda/\lambda 1$ at the margin is typical of folding of a decoupled lithosphere (Fig. 7) whereas $\lambda 2$ is more in line with a model of lithospheric folding for the whole continental lithosphere (Fig. 7). Although subject to uncertainties, our models confirm the concept that deformation during passive margin inversion occurs over a wide area, that is reduced in size during underthrusting stage.

6. Conclusions

Our physical analogue models focus on the mechanisms and deformational response during the process of passive margin inversion. Our study shows that both the décollement at the base of the ductile crust and the strength of the viscous mantle lithosphere are key elements for creating an instability at the passive margin. Experimental results show that intermediate strength of ductile mantle lithospheres (i. e. with a mean viscosity η of 5.8×10^{21} Pa s) favors deformation of the passive margin whereas a low strength mantle lithosphere (η of 1.7×10^{21} Pa s) leads to unstable intra-oceanic subduction and a strong mantle

lithosphere (η of 1.4×10^{22} Pa s or larger) to lithosphere folding.

Passive margin inversion for favourable mechanical conditions includes three stages: i) widespread deformation of continental crust at the passive margin by folding ii) deformation that is confined to the passive margin where shortening is accommodated by a continent-ward propagating thrust system that evolves from and roots in a decollement at the base of the ductile passive margin crust facilitating underthrusting of the oceanic plate, and iii) subduction of the oceanic lithosphere. These evolutionary stages are characterized by a 35–50% reduction of deformation width documenting the switch from distributed deformation (stage I) to localized deformation (stages II and III).

On the basis of our experimental results, we constrain early stage length scales of deformation at passive margin to predict the likeliness of subduction initiation. Our models predict that underthrusting would occur in case of folding at passive margin over a distance of $\lambda = 100–300$ km, whereas short ($\lambda = 50–100$ km) and long wavelength foldings ($\lambda = 500–1000$ km) are characteristic of intra-oceanic underthrusting and continental lithosphere folding, respectively. Our results are consistent with length-scales of deformation of natural inverted passive margins and allow for narrowing down favourable mechanical conditions for subduction initiation.

Acknowledgements, samples, and data

This manuscript is dedicated to our dear colleague, co-author and friend J.P. Brun. The constructive comments of Zhong-Hai Li and Laëtitia Le Pourhiet significantly helped to improve the manuscript. Data to support this article are available at the Yoda data repository at Utrecht University, Doi:10.24416/UU01-CMK25L. Surface Images have been processed with the software Surfer from Golden Software, LLC. We acknowledge the use of imagery from the NASA Worldview application (https://worldview.earthdata.nasa.gov), part of the NASA Earth Observing System Data and Information System (EOSDIS). This research project was funded by the European Union's EU Framework Programme for Research and Innovation Horizon 2020 "Subitop" under Grant Agreement No 674899.

Declaration of Competing Interest

None

Appendix A. Supplementary data

Supplementary data to this article can be found online at https://doi.org/10.1016/j.tecto.2021.229042.

References

Afonso, JC, Ranalli, Giorgio, Fernandez, M, 2007. Density structure and buoyancy of the oceanic lithosphere revisited. Geophysical Research Letters 34 (10).
Alvarez-Marron, J., Rubio, E., Torne, M., 1997. Subduction-related structures in the North Iberian margin. J. Geophys. Res. Solid Earth 102 (B10), 22497–22511. https://doi.org/10.1029/97JB01425.
Artemieva, I.M., 2009. The continental lithosphere: reconciling thermal, seismic, and petrologic data. Lithos 109 (1–2), 23–46.
Assumpcao, M., 1992. The regional intraplate stress field in South America. J. Geophys. Res. Solid Earth 97 (B8), 11889–11903.
Assumpção, M., Sacek, V., 2013. Intra-plate seismicity and flexural stresses in Central Brazil. Geophys. Res. Lett. 40 (3), 487–491. https://doi.org/10.1002/grl.50142.
Auzemery, A., Willingshofer, E., Yamato, P., Duretz, T., Sokoutis, D., 2020. Strain localization mechanisms for subduction initiation at passive margins. Glob. Planet. Chang. https://doi.org/10.1016/j.gloplacha.2020.103323.
Baes, M., Sobolev, S.V., Quinteros, J., 2018. Subduction initiation in mid-ocean induced by mantle suction flow. Geophys. J. Int. 215 (3), 1515–1522.
Barros, L.V., Assumpção, M., Quintero, R., Caixeta, D., 2009. The intraplate Porto dos Gaúchos seismic zone in the Amazon craton—Brazil. Tectonophysics 469 (1–4), 37–47.
Bauer, K., Neben, S., Schreckenberger, B., Emmermann, R., Hinz, K., Fechner, N., Gohl, K., Schulze, A., Trumbull, R.B., Weber, K., 2000. Deep structure of the Namibia continental margin as derived from integrated geophysical studies. J. Geophys. Res. Solid Earth 105 (B11), 25829–25853.
Beekman, F., Bull, J.M., Cloetingh, S., Scrutton, R., 1996. Crustal fault reactivation facilitating lithospheric folding/buckling in the Central Indian Ocean. Geol. Soc. Lond., Spec. Publ. 99 (1), 251–263.
Benhenni, L., Quesnel, Y., Berguig, M., Samai, S., Hamoudi, M., 2019. Joint modeling of potential-field data and geodynamic interpretation for northeast Algeria. J. Afr. Earth Sci. 159, 103566.
Billen, M.I., Hirth, G., 2005. Newtonian versus non-Newtonian upper mantle viscosity: Implications for subduction initiation. Geophys. Res. Lett. 32 (19).
Bills, B.G., Currey, D.R., Marshall, G.A., 1994. Viscosity estimates for the crust and upper mantle from patterns of lacustrine shoreline deformation in the Eastern Great Basin. J. Geophys. Res. Solid Earth 99 (B11), 22059–22086.
Bonnet, S., Guillocheau, F., Brun, J.P., Van Den Driessche, J., 2000. Large-scale relief development related to Quaternary tectonic uplift of a Proterozoic-Paleozoic basement: the Armorican Massif, NW France. J. Geophys. Res. Solid Earth 105 (B8), 19273–19288.
Boonma, K., Kumar, A., García-Castellanos, D., Jiménez-Munt, I., Fernández, M., 2019. Lithospheric mantle buoyancy: the role of tectonic convergence and mantle composition. Sci. Rep. 9 (1), 1–8.
Bourgeois, O., Ford, M., Diraison, M., De Veslud, C.L.C., Gerbault, M., Pik, R., Ruby, N., Bonnet, S., 2007. Separation of rifting and lithospheric folding signatures in the NW-Alpine foreland. Int. J. Earth Sci. 96 (6), 1003–1031.
Brace, W., Kohlstedt, D., 1980. Limits on lithospheric stress imposed by laboratory experiments. J. Geophys. Res. Solid Earth 85 (B11), 6248–6252.
Bradley, D.C., 2008. Passive margins through earth history. Earth Sci. Rev. 91 (1–4), 1–26.
Broerse, T., Norder, B., Govers, R., Sokoutis, D., Willingshofer, E., Picken, S.J., 2019. New analogue materials for nonlinear lithosphere rheology, with an application to slab break-off. Tectonophysics 756, 73–96.
Brun, J.P., 1999. Narrow rifts versus wide rifts: inferences for the mechanics of rifting from laboratory experiments. Philos. Trans. Roy Soc. Lond. A 357, 695–712 (1753).
Brun, J.-P., 2002. Deformation of the continental lithosphere: Insights from brittle-ductile models. Geol. Soc. Lond., Spec. Publ. 200 (1), 355–370.
Buck, W.R., 1991. Modes of continental lithospheric extension. J. Geophys. Res. Solid Earth 96 (B12), 20161–20178. https://doi.org/10.1029/91JB01485.
Burke, K., 1976. The Chad Basin: an active intra-continental basin. In: Developments in Geotectonics, Vol. 12. Elsevier, pp. 197–206.
Burov, E.B., 2011. Rheology and strength of the lithosphere. Mar. Pet. Geol. 28 (8), 1402–1443.
Burov, E., Cloetingh, S., 2010. Plume-like upper mantle instabilities drive subduction initiation. Geophys. Res. Lett. 37 (3).
Burov, E.B., Diament, M., 1995. The effective elastic thickness (T e) of continental lithosphere: what does it really mean? J. Geophys. Res. Solid Earth 100 (B3), 3905–3927.
Calignano, E., Sokoutis, D., Willingshofer, E., Gueydan, F., Cloetingh, S., 2015. Asymmetric vs. symmetric deep lithospheric architecture of intra-plate continental orogens. Earth Planet. Sci. Lett. 424, 38–50.
Célérier, J., Sandiford, M., Hansen, D.L., Quigley, M., 2005. Modes of active intraplate deformation, Flinders Ranges, Australia. Tectonics 24 (6).
Chapman, D.S., Pollack, H.N., 1977. Regional geotherms and lithospheric thickness. Geology 5 (5), 265–268.
Chemenda, A.I., Mattauer, M., Bokun, A.N., 1996. Continental subduction and a mechanism for exhumation of high-pressure metamorphic rocks: new modelling and field data from Oman. Earth Planet. Sci. Lett. 143 (1–4), 173–182.
Chenin, P., Picazo, S., Jammes, S., Manatschal, G., Müntener, O., Karner, G., 2019. Potential role of lithospheric mantle composition in the Wilson cycle: a North Atlantic perspective. Geol. Soc. Lond., Spec. Publ. 470 (1), 157–172.
Chimpliganond, C., Assumpção, M., Von Huelsen, M., França, G.S., 2010. The intracratonic Caraíbas–Itacarambi earthquake of December 09, 2007 (4.9 mb), Minas Gerais State, Brazil. Tectonophysics 480 (1–4), 48–56.
Chulick, G.S., Detweiler, S., Mooney, W.D., 2013. Seismic structure of the crust and uppermost mantle of South America and surrounding oceanic basins. J. S. Am. Earth Sci. 42, 260–276.
Cloetingh, S., Burov, E., 2011. Lithospheric folding and sedimentary basin evolution: a review and analysis of formation mechanisms. Basin Res. 23 (3), 257–290. https://doi.org/10.1111/j.1365-2117.2010.00490.x.
Cloetingh, S.A.P.L., Wortel, M., Vlaar, N., 1982. Evolution of passive continental margins and initiation of subduction zones. Nature 297 (5862), 139.
Cloetingh, S., Wortel, M., Vlaar, N., 1984. Passive margin evolution, initiation of subduction and the Wilson cycle. In: Zwart, H., Behr, H., JE, O. (Eds.), Tectonophysics, Vol. 109, pp. 147–163.
Cloetingh, S., Wortel, R., Vlaar, N., 1989. On the initiation of subduction zones. In: Subduction Zones Part II. Birkhauser Verlag, pp. 7–25.
Cloetingh, S., Burov, E., Poliakov, A., 1999. Lithosphere folding: primary response to compression? (from Central Asia to Paris basin). Tectonics 18 (6), 1064–1083. https://doi.org/10.1029/1999tc900040.
Cloetingh, S., Beekman, F., Ziegler, P.A., van Wees, J.-D., Sokoutis, D., 2008. Post-rift compressional reactivation potential of passive margins and extensional basins. Geol. Soc. Lond., Spec. Publ. 306 (1), 27–70.
Coblentz, D.D., Richardson, R.M., 1996. Analysis of the south American intraplate stress field. J. Geophys. Res. Solid Earth 101 (B4), 8643–8657.
Cogné, N., Gallagher, K., Cobbold, P.R., Riccomini, C., Gautheron, C., 2012. Post-breakup tectonics in southeast Brazil from thermochronological data and combined inverse-forward thermal history modeling. J. Geophys. Res. Solid Earth 117 (B11).
Crameri, F., Magni, V., Domeier, M., Shephard, G.E., Chotalia, K., Cooper, G., Eakin, C. M., Grima, A.G., Gürer, D., Király, Á., 2020. A transdisciplinary and community-driven database to unravel subduction zone initiation. Nat. Commun. 11 (1), 1–14.

Davy, P., Cobbold, P., 1991. Experiments on shortening of a 4-layer model of the continental lithosphere. Tectonophysics 188 (1–2), 1–25.
de Lima, C.C., 2000. Ongoing compression across intraplate South America: observations and some implications for petroleum exploitation and exploration. Revista Brasileira de Geociências 30 (1), 203–207.
De Vicente, G., Vegas, R., 2009. Large-scale distributed deformation controlled topography along the western Africa–Eurasia limit: tectonic constraints. Tectonophysics 474 (1–2), 124–143.
Dixon, J.E., Dixon, T.H., Bell, D., Malservisi, R., 2004. Lateral variation in upper mantle viscosity: role of water. Earth Planet. Sci. Lett. 222 (2), 451–467.
Dombrádi, E., Sokoutis, D., Bada, G., Cloetingh, S., Horváth, F., 2010. Modelling recent deformation of the Pannonian lithosphere: lithospheric folding and tectonic topography. Tectonophysics 484 (1–4), 103–118.
Duarte, J.C., Rosas, F.M., Terrinha, P., Schellart, W.P., Boutelier, D., Gutscher, M.-A., Ribeiro, A., 2013. Are subduction zones invading the Atlantic? Evidence from the Southwest Iberia margin. Geology 41 (8), 839–842.
Duretz, T., Petri, B., Mohn, G., Schmalholz, S., Schenker, F., Müntener, O., 2016. The importance of structural softening for the evolution and architecture of passive margins. Sci. Rep. 6 (1), 1–7.
England, P., Wortel, R., 1980. Some consequences of the subduction of young slabs. Earth Planet. Sci. Lett. 47 (3), 403–415.
Faccenna, C., Giardini, D., Davy, P., Argentieri, A., 1999. Initiation of subduction at Atlantic-type margins: insights from laboratory experiments. J. Geophys. Res. Solid Earth 104 (B2), 2749–2766.
Ferreira, J.M., Oliveira, T., Takeya, M.K., Assumpção, M., 1998. Superposition of local and regional stresses in Northeast Brazil: evidence from focal mechanisms around the Potiguar marginal basin. Geophys. J. Int. 134 (2), 341–355.
Gerya, T.V., Connolly, J.A., Yuen, D.A., 2008. Why is terrestrial subduction one-sided? Geology 36 (1), 43–46.
Gerya, T.V., Stern, R.J., Baes, M., Sobolev, S.V., Whattam, S.A., 2015. Plate tectonics on the Earth triggered by plume-induced subduction initiation. Nature 527 (7577), 221–225.
Göğüş, O.H., Pysklywec, R.N., 2008. Near-surface diagnostics of dripping or delaminating lithosphere. J. Geophys. Res. Solid Earth 113 (B11).
Goren, L., Aharonov, E., Mulugeta, G., Koyi, H.A., Mart, Y., 2008. Ductile deformation of passive margins: a new mechanism for subduction initiation. J. Geophys. Res. Solid Earth 113 (B8). https://doi.org/10.1029/2005JB004179.
Gurnis, M., Hall, C., Lavier, L., 2004. Evolving force balance during incipient subduction. Geochem. Geophys. Geosyst. 5 (7).
Hall, R., 2019. The subduction initiation stage of the Wilson cycle. Geol. Soc. Lond., Spec. Publ. 470 (1), 415–437.
Hamai, L., Petit, C., Abtout, A., Yelles-Chaouche, A., Déverchère, J., 2015. Flexural behaviour of the north Algerian margin and tectonic implications. Geophys. J. Int. 201 (3), 1426–1436.
Hamai, L., Petit, C., Le Pourhiet, L., Yelles-Chaouche, A., Déverchère, J., Beslier, M.-O., Abtout, A., 2018. Towards subduction inception along the inverted North African margin of Algeria? Insights from thermo-mechanical models. Earth Planet. Sci. Lett. 501, 13–23.
Hirth, G., Kohlstedt, D., 2003. Rheology of the upper mantle and the mantle wedge: A view from the experimentalists. Inside the Subduction Factory 83–105.
Holford, S.P., Green, P.F., Duddy, I.R., Turner, J.P., Hillis, R.R., Stoker, M.S., 2009. Regional intraplate exhumation episodes related to plate-boundary deformation. Geol. Soc. Am. Bull. 121 (11–12), 1611–1628.
Holford, S., Hillis, R., Duddy, I., Green, P., Stoker, M., Tuitt, A., Backé, G., Tassone, D., MacDonald, J., 2011. Cenozoic post-breakup compressional deformation and exhumation of the southern Australian margin. APPEA J. 51 (1), 613–638.
Hubbert, M.K., 1937. Theory of scale models as applied to the study of geologic structures. Bull. Geol. Soc. Am. 48 (10), 1459–1520.
Jaeger, J.C., Cook, N.G., Zimmerman, R., 2009. Fundamentals of Rock Mechanics. John Wiley & Sons.
Jammes, Suzon, Lavier, Luc, 2016. The effect of bimineralic composition on extensional processes at lithospheric scale. Geochemistry, Geophysics, Geosystems 17 (8), 3375–3392.
Johnson, H., 2008. The Nature and Origin of Compression in Passive Margins.
Karner, G., Watts, A., 1983. Gravity anomalies and flexure of the lithosphere at mountain ranges. J. Geophys. Res. Solid Earth 88 (B12), 10449–10477.
Kaufmann, G., Amelung, F., 2000. Reservoir-induced deformation and continental rheology in vicinity of Lake Mead, Nevada. J. Geophys. Res. Solid Earth 105 (B7), 16341–16358.
Keep, M., Harrowfield, M., 2008. Elastic flexure and distributed deformation along Australia's North West Shelf: Neogene tectonics of the Bonaparte and Browse basins. Geol. Soc. Lond., Spec. Publ. 306 (1), 185–200.
Kim, G.-B., Yoon, S.-H., Kim, S.-S., So, B.-D., 2018. Transition from buckling to subduction on strike-slip continental margins: evidence from the East Sea (Japan Sea). Geology 46 (7), 603–606. https://doi.org/10.1130/g40305.1.
Kirby, S.H., 1985. Rock mechanics observations pertinent to the rheology of the continental lithosphere and the localization of strain along shear zones. Tectonophysics 119 (1–4), 1–27.
Kiss, D., Candioti, L.G., Duretz, T., Schmalholz, S.M., 2020. Thermal softening induced subduction initiation at a passive margin. Geophys. J. Int. 220 (3), 2068–2073.
Leprêtre, A., Klingelhoefer, F., Graindorge, D., Schnurle, P., Beslier, M.O., Yelles, K., Déverchère, J., Bracene, R., 2013. Multiphased tectonic evolution of the Central Algerian margin from combined wide-angle and reflection seismic data off Tipaza, Algeria. J. Geophys. Res. Solid Earth 118 (8), 3899–3916. https://doi.org/10.1002/jgrb.50318.
Leroy, M., Dauteuil, O., Cobbold, P.R., 2004. Incipient shortening of a passive margin: the mechanical roles of continental and oceanic lithospheres. Geophys. J. Int. 159 (1), 400–411.
Li, L., Stephenson, R., Clift, P.D., 2016a. The Canada Basin compared to the southwest South China Sea: two marginal ocean basins with hyper-extended continent-ocean transitions. Tectonophysics 691, 171–184.
Li, Z.H., Liu, M., Gerya, T., 2016b. Lithosphere delamination in continental collisional orogens: a systematic numerical study. J. Geophys. Res. Solid Earth 121 (7), 5186–5211.
Løseth, H., Henriksen, S., 2005. A Middle to late Miocene compression phase along the Norwegian passive margin. In: Paper Presented at the Geological Society, London, Petroleum Geology Conference series.
Lundin, E., Doré, A., 2002. Mid-Cenozoic post-breakup deformation in the 'passive'margins bordering the Norwegian–Greenland Sea. Mar. Pet. Geol. 19 (1), 79–93.
Luth, S., Willingshofer, E., Sokoutis, D., Cloetingh, S., 2010. Analogue modelling of continental collision: Influence of plate coupling on mantle lithosphere subduction, crustal deformation and surface topography. Tectonophysics 484 (1–4), 87–102.
Maffione, M., Thieulot, C., Van Hinsbergen, D.J., Morris, A., Plümper, O., Spakman, W., 2015. Dynamics of intraoceanic subduction initiation: 1. Oceanic detachment fault inversion and the formation of supra-subduction zone ophiolites. Geochem. Geophys. Geosyst. 16 (6), 1753–1770.
Malavieille, J., 2010. Impact of erosion, sedimentation, and structural heritage on the structure and kinematics of orogenic wedges: analog models and case studies. GSA Today 20 (1), 4–10.
Manzotti, P., Ballevre, M., Zucali, M., Robyr, M., Engi, M., 2014. The tectonometamorphic evolution of the Sesia–Dent Blanche nappes (internal Western Alps): review and synthesis. Swiss J. Geosci. 107 (2–3), 309–336.
Mart, Y., Aharonov, E., Mulugeta, G., Ryan, W., Tentler, T., Goren, L., 2005. Analogue modelling of the initiation of subduction. Geophys. J. Int. 160 (3), 1081–1091. https://doi.org/10.1111/j.1365-246X.2005.02544.x.
Martinod, J., Davy, P., 1992. Periodic instabilities during compression or extension of the lithosphere 1. Deformation modes from an analytical perturbation method. J. Geophys. Res. Solid Earth 97 (B2), 1999–2014.
Maystrenko, Y., Scheck-Wenderoth, M., 2009. Density contrasts in the upper mantle and lower crust across the continent—ocean transition: constraints from 3-D gravity modelling at the Norwegian margin. Geophys. J. Int. 179 (1), 536–548.
Maystrenko, Y.P., Scheck-Wenderoth, M., Hartwig, A., Anka, Z., Watts, A.B., Hirsch, K.K., Fishwick, S., 2013. Structural features of the Southwest African continental margin according to results of lithosphere-scale 3D gravity and thermal modelling. Tectonophysics 604, 104–121. https://doi.org/10.1016/j.tecto.2013.04.014.
McAdoo, D.C., Sandwell, D.T., 1985. Folding of oceanic lithosphere. J. Geophys. Res. Solid Earth 90 (B10), 8563–8569.
McCarthy, A., Chelle-Michou, C., Müntener, O., Arculus, R., Blundy, J., 2018. Subduction initiation without magmatism: the case of the missing Alpine magmatic arc. Geology 46 (12), 1059–1062.
Midtkandal, I., Brun, J.-P., Gabrielsen, R.H., Huismans, R.S., 2013. Control of lithosphere rheology on subduction polarity at initiation: Insights from 3D analogue modelling. Earth Planet. Sci. Lett. 361, 219–228.
Milani, E., Zalán, P., 1998. *Brazilian Geology Part I: The geology of Paleozoic cratonic basins and Mesozoic interior rifts of Brazil.* Paper presented at the 1998 AAPG International Conference and Exhibition, Rio de Janeiro, Brazil, Short Course Notes.
Modenesi-Gauttieri, M.C., De Toledo, M.C.M., Hiruma, S.T., Taioli, F., Shimada, H., 2011. Deep weathering and landscape evolution in a tropical plateau. Catena 85 (3), 221–230.
Monnereau, M., Rabinowicz, M., Arquis, E., 1993. Mechanical erosion and reheating of the lithosphere: a numerical model for hotspot swells. J. Geophys. Res. Solid Earth 98 (B1), 809–823.
Mueller, S., Phillips, R.J., 1991. On the initiation of subduction. J. Geophys. Res. Solid Earth 96 (B1), 651–665. https://doi.org/10.1029/90JB02237.
Müller, R.D., Sdrolias, M., Gaina, C., Roest, W.R., 2008. Age, spreading rates, and spreading asymmetry of the world's ocean crust. Geochem. Geophys. Geosyst. 9 (4).
Neto, H.C.L., Ferreira, J.M., Bezerra, F.H.R., Assumpção, M.S., do Nascimento, A. F., Sousa, M. O., & Menezes, E. A., 2013. Upper crustal earthquake swarms in São Caetano: Reactivation of the Pernambuco shear zone and trending branches in intraplate Brazil. Tectonophysics 608, 804–811.
Nikolaeva, K., Gerya, T.V., Marques, F.O., 2010. Subduction initiation at passive margins: numerical modeling. J. Geophys. Res. Solid Earth 115 (B3). https://doi.org/10.1029/2009JB006549.
Nikolaeva, K., Gerya, T.V., Marques, F.O., 2011. Numerical analysis of subduction initiation risk along the Atlantic American passive margins. Geology 39 (5), 463–466.
Osmundsen, P.T., Redfield, T.F., 2011. Crustal taper and topography at passive continental margins. Terra Nova 23 (6), 349–361. https://doi.org/10.1111/j.1365-3121.2011.01014.x.
Oxburgh, E., Turcotte, D., 1976. The physico-chemical behaviour of the descending lithosphere. Tectonophysics 32 (1–2), 107–128.
Pascal, C., Cloetingh, S.A., 2009. Gravitational potential stresses and stress field of passive continental margins: Insights from the South-Norway shelf. Earth Planet. Sci. Lett. 277 (3–4), 464–473.
Pedoja, K., Husson, L., Regard, V., Cobbold, P.R., Ostanciaux, E., Johnson, M.E., Kershaw, S., Saillard, M., Martinod, J., Furgerot, L., 2011. Relative sea-level fall since the last interglacial stage: are coasts uplifting worldwide? Earth Sci. Rev. 108 (1–2), 1–15.

Pedreira, D., Pulgar, J., Gallart, J., Torné, M., 2007. Three-dimensional gravity and magnetic modeling of crustal indentation and wedging in the western Pyrenees-Cantabrian Mountains. J. Geophys. Res. Solid Earth 112 (B12).
Petersen, K.D., Schiffer, C., 2016. Wilson cycle passive margins: Control of orogenic inheritance on continental breakup. Gondwana Res. 39, 131–144.
Pinto, L.G.R., de Pádua, M.B., Ussami, N., Vitorello, Í., Padilha, A.L., Braitenberg, C., 2010. Magnetotelluric deep soundings, gravity and geoid in the South São Francisco craton: Geophysical indicators of cratonic lithosphere rejuvenation and crustal underplating. Earth Planet. Sci. Lett. 297 (3–4), 423–434.
Quigley, M.C., Clark, D., Sandiford, M., 2010. Tectonic geomorphology of Australia. Geol. Soc. Lond., Spec. Publ. 346 (1), 243–265.
Ramberg, H., 1981. Gravity, Deformation and the earth's Crust: In Theory, Experiments and Geological Application. Academic Press.
Ranalli, G., 1995. Rheology of the Earth. Springer Science & Business Media.
Regenauer-Lieb, K., Yuen, D.A., Branlund, J., 2001. The initiation of subduction: criticality by addition of water? Science 294 (5542), 578–580.
Reston, Tim, 2009. The structure, evolution and symmetry of the magma-poor rifted margins of the North and Central Atlantic: A synthesis. Tectonophysics 468, 6–27.
Reston, T., Manatschal, G., 2011. Rifted margins: Building blocks of later collision. In: Arc-Continent Collision. Springer, pp. 3–21.
Riccomini, C., Sant'Anna, L.G., Ferrari, A.L., 2004. Evolução geológica do rift continental do sudeste do Brasil. Geologia do continente Sul-Americano: evolução da obra de Fernando Flávio Marques de Almeida, pp. 383–405.
Rocha, M.P., de Azevedo, P.A., Marotta, G.S.A., Schimmel, M., Fuck, R., 2016. Causes of intraplate seismicity in central Brazil from travel time seismic tomography. Tectonophysics 680, 1–7.
Rolland, Y., Galoyan, G., Bosch, D., Sosson, M., Corsini, M., Fornari, M., Verati, C., 2009. Jurassic back-arc and cretaceous hot-spot series in the Armenian ophiolites—Implications for the obduction process. Lithos 112 (3–4), 163–187.
Roure, F., Casero, P., Addoum, B., 2012. Alpine inversion of the North African margin and delamination of its continental lithosphere. Tectonics 31 (3). https://doi.org/10.1029/2011TC002989.
Santimano, T., Pysklywec, R., 2020. The influence of lithospheric mantle scars and rheology on intraplate deformation and orogenesis: Insights from tectonic analog models. Tectonics *39* (5) e2019TC005841.
Schellart, W.P., Strak, V., 2016. A review of analogue modelling of geodynamic processes: approaches, scaling, materials and quantification, with an application to subduction experiments. J. Geodyn. 100, 7–32.
Sokoutis, D., Willingshofer, E., 2011. Decoupling during continental collision and intra-plate deformation. Earth Planet. Sci. Lett. 305 (3–4), 435–444.
Schubert, Gerald, Turcotte, Donald Lawson, Olson, Peter, 2001. Mantle convection in the Earth and planets. Cambridge University Press.
Sokoutis, D., Bonini, M., Medvedev, S., Boccaletti, M., Talbot, C.J., Koyi, H., 2000. Indentation of a continent with a built-in thickness change: experiment and nature. Tectonophysics 320 (3–4), 243–270.
Sokoutis, D., Burg, J.-P., Bonini, M., Corti, G., Cloetingh, S., 2005. Lithospheric-scale structures from the perspective of analogue continental collision. Tectonophysics 406 (1–2), 1–15.
Stanton, N., Kusznir, N., Gordon, A., Schmitt, R., 2019. Architecture and Tectono-magmatic evolution of the Campos Rifted Margin: control of OCT structure by basement inheritance. Mar. Pet. Geol. 100, 43–59.
Starostenko, V., Janik, T., Lysynchuk, D., Środa, P., Czuba, W., Kolomiyets, K., Aleksandrowski, P., Gintov, O., Omelchenko, V., Komminaho, K., Guterch, A., Tiira, T., Gryn, D., Legostaeva, O., Thybo, H., Tolkunov, A., 2013. Mesozoic(?) lithosphere-scale buckling of the East European Craton in southern Ukraine: DOBRE-4 deep seismic profile. Geophys. J. Int. 195 (2), 740–766. https://doi.org/10.1093/gji/ggt292.
Stein, C.A., Cloetingh, S., Wortel, R., 1989a. Seasat-derived gravity constraints on stress and deformation in the northeastern Indian Ocean. Geophys. Res. Lett. 16 (8), 823–826.
Stein, S., Cloetingh, S., Sleep, N.H., Wortel, R., 1989b. Passive margin earthquakes, stresses and rheology. In: Earthquakes at North-Atlantic Passive Margins: Neotectonics and Postglacial Rebound. Springer, pp. 231–259.
Stephenson, R., Cloetingh, S., 1991. Some examples and mechanical aspects of continental lithospheric folding. Tectonophysics 188 (1–2), 27–37.
Stern, R.J., 2004. Subduction initiation: spontaneous and induced. Earth Planet. Sci. Lett. 226 (3–4), 275–292.
Stern, R.J., Gerya, T., 2018. Subduction initiation in nature and models: A review. Tectonophysics 746, 173–198.
Strak, V., Schellart, W.P., 2018. A subduction and mantle plume origin for Samoan volcanism. Sci. Rep. 8 (1), 1–12.
Teixell, A., Labaume, P., Ayarza, P., Espurt, N., de Saint Blanquat, M., Lagabrielle, Y., 2018. Crustal structure and evolution of the Pyrenean-Cantabrian belt: a review and new interpretations from recent concepts and data. Tectonophysics 724, 146–170.
Thielmann, M., Kaus, B.J., 2012. Shear heating induced lithospheric-scale localization: does it result in subduction? Earth Planet. Sci. Lett. 359, 1–13.
Turcotte, D., Schubert, G., 2014. Geodynamics. Cambridge University Press.
Unternehr, P., Péron-Pinvidic, G., Manatschal, G., Sutra, E., 2010. Hyper-extended crust in the South Atlantic: in search of a model. Pet. Geosci. 16 (3), 207–215. https://doi.org/10.1144/1354-079309-904.
Ussami, N., Shiraiwa, S., Dominguez, J.M.L., 1999. Basement reactivation in a sub-Andean foreland flexural bulge: the Pantanal wetland, SW Brazil. Tectonics 18 (1), 25–39.
Van der Meijde, M., Julià, J., Assumpção, M., 2013. Gravity derived Moho for South America. Tectonophysics 609, 456–467.
Vergnolle, M., Pollitz, F., Calais, E., 2003. Constraints on the viscosity of the continental crust and mantle from GPS measurements and postseismic deformation models in western Mongolia. J. Geophys. Res. Solid Earth 108 (B10).
Viejo, G.F., Gallastegui, J., 2005. The ESCI-N Project after a decade: A síntesis of the results and open questions. Trab. Geol. 25 (25), 9–27.
Vlaar, N., Wortel, M., 1976. Lithospheric aging, instability and subduction. Tectonophysics 32 (3–4), 331–351.
Watts, A., Burov, E., 2003. Lithospheric strength and its relationship to the elastic and seismogenic layer thickness. Earth Planet. Sci. Lett. 213 (1–2), 113–131.
Watts, A., Zhong, S., Hunter, J., 2013. The behavior of the lithosphere on seismic to geologic timescales. Annu. Rev. Earth Planet. Sci. 41, 443–468.
Weertman, J., 1978. Creep laws for the mantle of the Earth. *Philosophical transactions of the Royal Society of London*. Series A, Math. Phys. Sci. 288 (1350), 9–26.
Weijermars, R., Schmeling, H., 1986. Scaling of Newtonian and non-Newtonian fluid dynamics without inertia for quantitative modelling of rock flow due to gravity (including the concept of rheological similarity). Phys. Earth Planet. Inter. 43 (4), 316–330.
Whattam, S.A., Stern, R.J., 2015. Late cretaceous plume-induced subduction initiation along the southern margin of the Caribbean and NW South America: the first documented example with implications for the onset of plate tectonics. Gondwana Res. 27 (1), 38–63.
Willett, S., Beaumont, C., Fullsack, P., 1993. Mechanical model for the tectonics of doubly vergent compressional orogens. Geology 21 (4), 371–374.
Willingshofer, E., Sokoutis, D., 2009. Decoupling along plate boundaries: key variable controlling the mode of deformation and the geometry of collisional mountain belts. Geology 37 (1), 39–42.
Willingshofer, E., Sokoutis, D., Burg, J.-P., 2005. Lithospheric-scale analogue modelling of collision zones with a pre-existing weak zone. Geol. Soc. Lond., Spec. Publ. 243 (1), 277–294.
Willingshofer, E., Sokoutis, D., Luth, S., Beekman, F., Cloetingh, S., 2013. Subduction and deformation of the continental lithosphere in response to plate and crust-mantle coupling. Geology 41 (12), 1239–1242.
Wilson, J.T., 1968. Static or mobile earth: the current scientific revolution. Proc. Am. Philos. Soc. 112 (5), 309–320.
Yamato, P., Husson, L., Becker, T.W., Pedoja, K., 2013. Passive margins getting squeezed in the mantle convection vice. Tectonics 32 (6), 1559–1570. https://doi.org/10.1002/2013TC003375.
Zhong, X., Li, Z.H., 2019. Forced subduction initiation at passive continental margins: velocity-driven versus stress-driven. Geophys. Res. Lett. 46 (20), 11054–11064.
Zhong, X., Li, Z.H., 2020. Subduction initiation during collision-induced subduction transference: numerical modeling and implications for the tethyan evolution. J. Geophys. Res. Solid Earth 125 (2) e2019JB019288.
Zhou, X., Li, Z.-H., Gerya, T.V., Stern, R.J., 2020. Lateral propagation–induced subduction initiation at passive continental margins controlled by preexisting lithospheric weakness. Sci. Adv. 6 (10) eaaz1048.
Ziegler, P.A., Cloetingh, S., 2004. Dynamic processes controlling evolution of rifted basins. Earth Sci. Rev. 64 (1–2), 1–50.
Ziegler, P.A., Cloetingh, S., van Wees, J.-D., 1995. Dynamics of intra-plate compressional deformation: the Alpine foreland and other examples. Tectonophysics 252 (1–4), 7–59.